PART III.

INTER-DEPARTMENTAL RESEARCH ACTIVITIES – SELECTED HIGHLIGHTS

Combining Identical Location Microscopy, Atom Probe Tomography and a Scanning-Flow Cell coupled with an Inductively Coupled Plasma Mass Spectrometer to Understand the Structure-Property of Catalysts

O. Kasian [1], B. Gault [2], T. Li [3], S. Zhang [4], S. Cherevko [5], C. Scheu [4], D. Raabe [2], G. Dehm [6], K. Mayrhofer [1, 5]

[1]Department of Interface Chemistry and Surface Engineering (GO)
[2] Department of Microstructure Physics and Alloy Design (MA)
[3] now at: Ruhr-Universität Bochum
[4] Independent Max Planck Research Group on Nanoanalytics and Interfaces (NG)
[5] now at: Helmholtz Institute Erlangen-Nürnberg for Renewable Energies
[6] Department of Structure and Nano-/ Micromechanics of Materials (SN)

Electrocatalysis is key to clean energy conversion and storage technologies. During electrocatalytic reactions the surface composition of electrodes undergoes drastic changes that lead to efficiency decrease and structural degradation [1]. Up to now, particularly for the important oxygen evolution reaction (OER) on oxidic surfaces, the mechanisms underpinning the transformations and their influence on the reactivity and durability of catalysts remained largely unknown [2], mainly due to limitations in sufficiently analytically sensitive surface probing techniques. The resulting knowledge gap regarding the question how the topmost atomic layers behave and compositionally change, has hindered the development of high-performance, long-lasting electrocatalysts.

A close collaboration between the departments GO, MA, SN and the NG group was established, with the aim to develop an approach to characterize the temporal evolution of the topmost atomic layers of catalysts in operation. Iridium oxide formed on pure iridium films by anodic electrochemical oxidation OER was chosen as a model system. Advanced activity-stability analyses were performed by scanning flow cell connected to an inductively coupled plasma mass spectrometer (SFC-ICP-MS). In parallel, we performed high-end near-atomic-scale characterization by atom probe tomography (APT) and (scanning) transmission electron microscopy ((S)TEM), electron energy loss spectroscopy (EELS) and X-ray photoelectron spectroscopy (XPS). In addition, to resolve

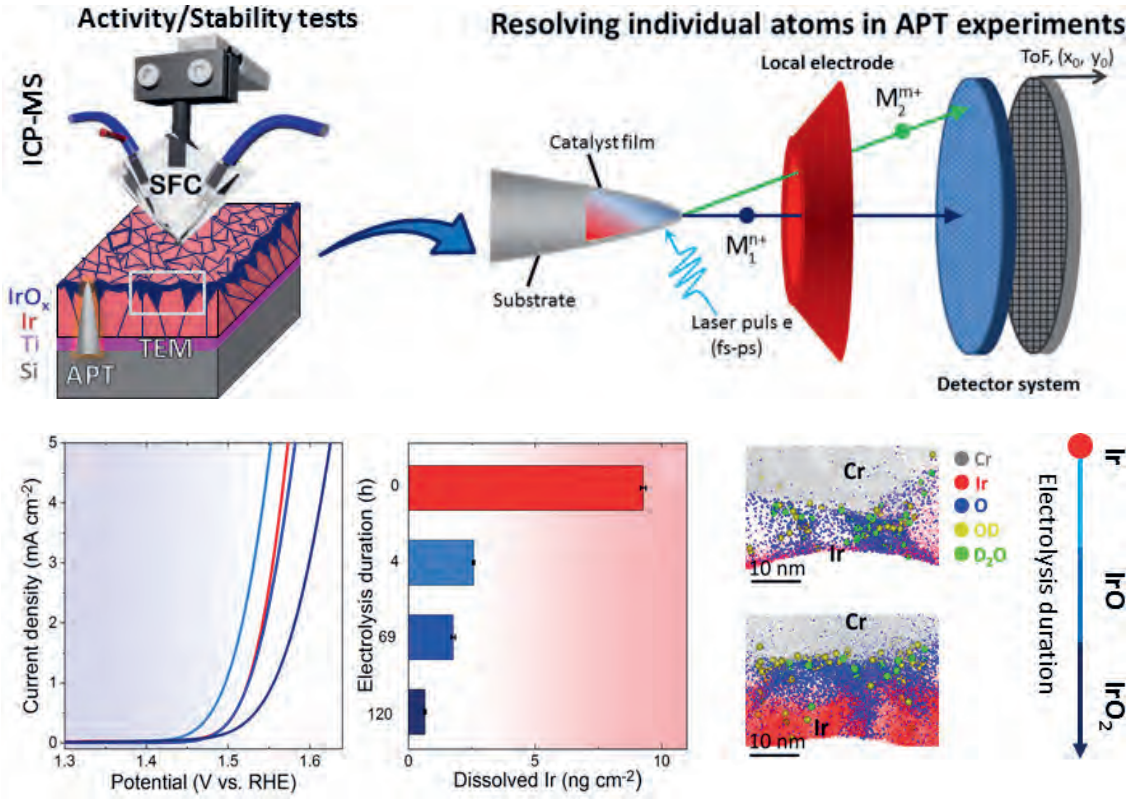

Fig. 1: *Combining SFC-ICP-MS with STEM and APT advanced understanding of electrocatalytic behaviour of Iridium OER catalysts.*

hydroxy-groups by APT in the electrochemically-grown oxides, proton-free deuterated electrolytes were used to avoid overlap with residual hydrogen from the ultra-high vacuum chamber.

This joint effort and the advanced characterization approach (Fig. 1) enabled to discover the formation of non-stoichiometric Ir-O species mixed with hydroxy-groups and water molecules during the short term electrolysis, providing a high electrocatalytic activity. The metastable Ir-O species gradually transform into IrO_2, which enabled to explain the observed decrease in activity and increase in stability [3]. The insights on the three-dimensional compositional distribution provided unique evidence of the chemical species residing at or near the outermost surface of Ir oxides and their transformation at near-atomic scale, which is critical for understanding the interplay between composition, reactivity and stability in electrocatalysis. In the future, this unique approach will be extended to other catalytic reactions and systems beyond OER and Ir-oxides. Combining advanced electrochemistry with APT and Identical Location Microscopy [4] will aid in unravelling the dynamic evolution of different nanoparticle catalysts commonly used in state of the art energy conversion and storage devices.

References

1. Pizzutilo, E.; Freakley, S.J.; Cherevko, S.; Venkatesan, S.; Hutchings, G.J.; Liebscher, C.H.; Dehm, G.; Mayrhofer, K.J.J.: ACS Catal 7 (2017) 5699.
2. Kasian, O.; Grote, J.P.; Geiger, S.; Cherevko, S.; Mayrhofer, K.J.J.: Angew Chem Int Edit 57 (2018) 2488.
3. Li, T.; Kasian, O.; Cherevko, S.; Zhang, S.; Geiger, S.; Scheu, C.; Felfer, P.; Raabe, D.; Gault, B.; Mayrhofer, K.J.J.: Nature Catal 1 (2018) 300.
4. Hodnik, N.; Gerhard, D.; Mayrhofer, K.J.J.: Accounts Chem Res 49 (2016) 2015.

Electrochemical Semiconductor/Water Interfaces

L. Yang [1], F. Niu [1], A. Erbe [1], S. Wippermann [1], M. Todorova [2], J. Neugebauer [2]

[1] *Department of Interface Chemistry and Surface Engineering (GO)*
[2] *Department of Computational Materials Design (CM)*

Solid/liquid interfaces are of ubiquitous importance, e.g., in electrochemistry, electrocatalysis and corrosion. Often, metal electrodes are covered by semiconducting oxide films, and oxide/water interfaces also form as a consequence of corrosion processes. Emerging photoelectrochemical technologies, such as light-induced water splitting, employ semiconducting photoelectrodes. Therefore, many electrochemical interfaces of interest are in fact semiconductor/liquid interfaces. We utilize single-crystalline, atomically flat interfaces between semiconductors and liquid water as well-defined model systems to develop and validate methods, and to understand fundamental principles and processes.

Hydrogenated silicon and germanium surfaces in contact with liquid water are of particular interest in this context. They are transparent with respect to infrared light. Thus, optical fingerprints of electrochemical reactions and intermediates can be obtained in operando using attenuated total reflection infrared (ATRIR) spectroscopy. In water, silicon is known to irreversibly form porous oxide layers. The exact oxidation mechanism, however, is not yet understood. In addition, oxidation can be suppressed completely or allowed to proceed at controlled rates depending on the potential applied to the silicon electrode. Silicon is therefore of interest as a model system for corrosion. On the other hand, we find that germanium features a reversible potential-induced phase transition of the surface termination. It is therefore of interest as a model system to develop methods for predicting surface Pourbaix diagrams from first principles.

We use the modern theory of polarization, which introduces an electric field term directly into the density-functional theory (DFT) Hamiltonian, to describe electric fields in *ab initio* molecular dynamics (MD) simulations. Thereby, we can simulate the full electrochemical cell without a vacuum region. On the time scales accessible to our *ab initio* simulations, MD calculations demonstrate the solvated Si(100):H surface to be stable in the absence of applied electric fields and no interfacial reactions are observed. Once, however, the field is switched on, we observe characteristic field-induced surface reactions within a few ps, cf. Fig. 1: on the positively charged anodic surface, a H_2O molecule dissociates (a). The H^+ is transferred to a neighbouring H_2O molecule, whereas the OH^- group binds to a surface Si atom, breaking a Si-Si backbond in the process (b). The proton is transported in accordance with the Grotthus mechanism towards the cathodic surface (c), where, at later

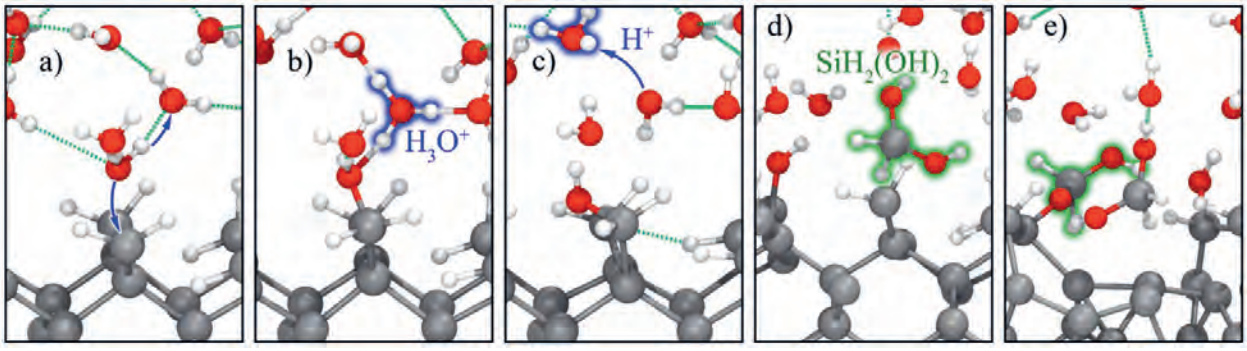

Fig. 1: *Snapshots of an ab initio MD simulation with applied electric field, showing initial oxidation steps of the solvated Si(100):H surface under anodic conditions, see text.*

stages when a sufficient number of protons has arrived, hydrogen evolution is observed. Eventually, a second water molecule dissociates and breaks the remaining Si-Si backbond of the surface SiH_2OH group. The resulting $SiH_2(OH)_2$ molecule is then solvated (d). Often, an OH group within the solvated $SiH_2(OH)_2$ molecule deprotonates and subsequently binds to another surface Si atom, forming an Si-O-Si bridge (e). These are the first steps towards electrochemical oxidation of Si.

On the Ge(100):H surface, a qualitatively different process emerges. Following the approach outlined by Surendralal et al. [1], we introduced a potentiostat directly into the Quantum Espresso DFT package and perform MD simulations at constant electrode potential. At each *ab initio* MD time step, the electric field is adjusted so as to keep the potential difference at a target value of -1 V. A damping term is introduced to prevent any abrupt changes of the field, changing the electric field in a smooth and adiabatic way at all times. Fig. 2a shows the surface charge and the potential difference between the Ge surface and a computational counter electrode as a function of time.

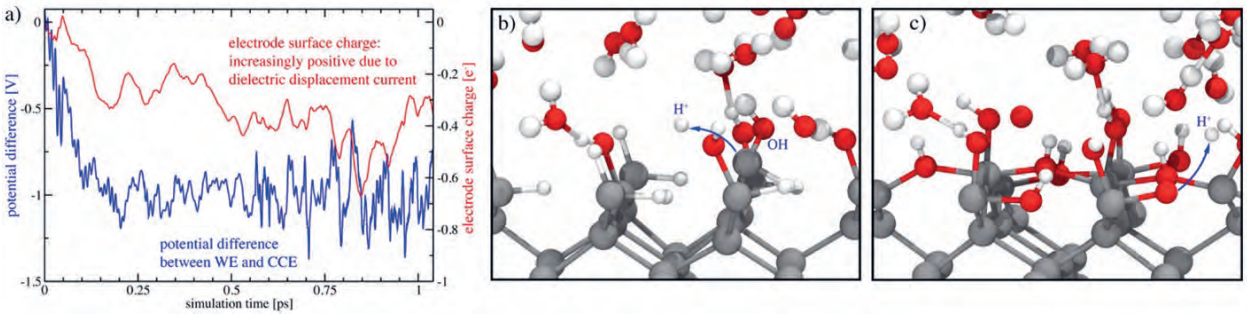

Fig. 2: *a) Surface charge and electrode potential as a function of time during ab initio MD simulations of solvated Ge(100):H surface. MD Snapshots of b) hydroxylation and c) oxidation events.*

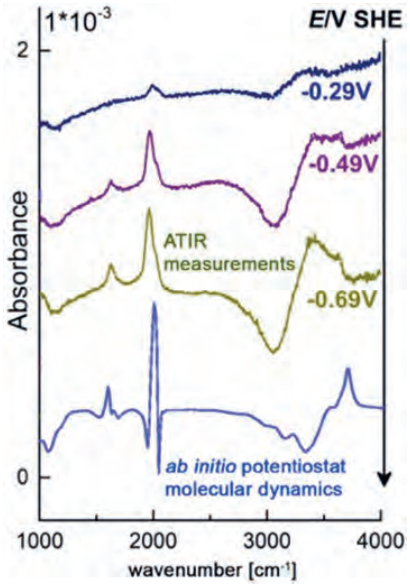

Fig. 3: *Infrared spectra of the Ge(100):H/H_2O interface, measured by ATRIR spectroscopy and compared to predictions from ab initio potentiostat MD simulations.*

To keep the electrode potential constant, save for thermal fluctuations, the potentiostat must, however, continuously adjust the surface charge towards increasingly anodic conditions. We are thus observing a dielectric displacement current, caused by water reorientation and formation of the electrochemical double layer. The increasing fluctuations observed after 0.75 ps are due to an OH^- ion approaching and attempting to hydroxylate the surface. A snapshot of the hydroxylation event is shown in Fig. 2b. On the completely hydroxylated surface the OH groups eventually move into the troughs between the rows of the surface Ge atoms and deprotonate, cf. Fig. 2c, and a thin surface oxide layer is formed.

Interestingly, in marked difference to our observations on Si(100):H, Ge hydroxylation and oxidation occur without breaking any Ge-Ge backbonds. The process thus resembles a surface phase transition. Indeed, ATRIR measurements confirm this transition to be potential-induced and reversible. Using our MD trajectories, we compute the difference between the vibrational spectra of the hydrogenated and hydroxylated Ge(100):H/H_2O interfaces. The resulting spectra are compared to ATRIR measurements in Fig. 3 [2]. The spectra predicted from first principles coincide closely with the ATRIR measurements, confirming the transition in surface termination observed in our potentiostat MD simulations.

These two examples demonstrate that with our new methodological advances it is now possible to perform *ab initio* molecular dynamics calculations with applied electric field and at constant electrode potential. They also illustrate how our continuous methodological developments help to reveal the fundamental mechanisms of electrochemical and corrosion reactions at solid/liquid interfaces.

References

1. Surendralal, S.; Todorova, M.; Finnis, M.; Neugebauer, J.: Phys Rev Lett 120 (2018) 246801.
2. Niu, F.; Schulz, R.; Castañeda Medina, A.; Schmid, R.; Erbe, A.: Phys Chem Chem Phys 19 (2017) 13585.

Passivity and Passivity Breakdown on Copper: Defect Formation during Oxygen Evolution and Effect of Chloride

C. Toparli [1,3], A. Sarfraz [1], S. Hieke [2], A. Altin [1], C. Scheu [2], A.D. Wieck [4], M. Rohwerder [1], A. Erbe [1,5]

[1] Department of Interface Chemistry and Surface Engineering (GO)
[2] Independent Max Planck Research Group on Nanoanalytics and Interfaces (NG)
[3] now at: Massachusetts Institute of Technology Cambridge, MA, USA
[4] Chair for Applied Solid State Physics, Ruhr-Universität Bochum
[5] Norwegian University of Science and Technology, Trondheim, Norway

Passivity breakdown is a major issue in corrosion. It is often assumed that passive films are simple, uniform and homogeneous oxide layers blocking the cation transfer from the metal surface to the electrolyte. However, recent advancement in surface analytical techniques show that almost all passive films have multilayer structure, including an inner layer, outer hydroxide part and also a barrier layer [1]. Passivity breakdown can occur due to several reasons during anodic polarisation up to the oxygen evolution reaction (OER). A key challenge remains the capture of the changes in the film *in situ* to obtain detailed insight into reactions. Aim of this work is to uncover passive film formation and its breakdown on Cu in relation to formation of point defects, electronic properties and chemical nature of oxides.

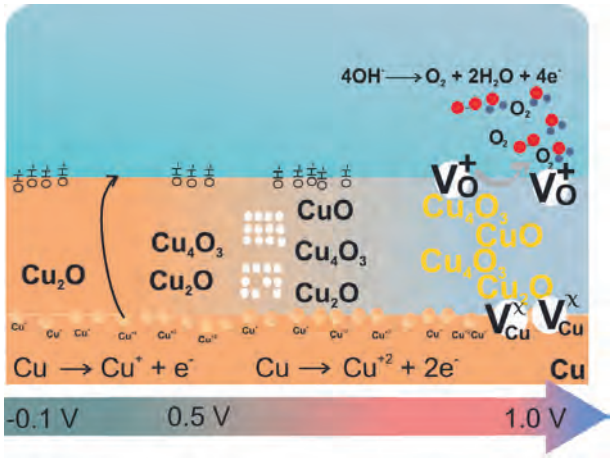

Fig. 1: *Scheme illustrating dominant oxide phases, and observed defect formation as function of electrode potential, on Cu in NaOH.*

In hydroxide, we systematically investigated the passive film formation, its breakdown accompanied by oxygen evolution, and the effect of Cl^- on passivity breakdown by *in situ* spectroscopic ellipsometry (SE), *in situ* Raman spectroscopy and *in situ* photoluminescence spectroscopy (PL), completed by *ex situ* techniques. The thickness of the passive oxide layers was calculated from SE data by a model-independant first order perturbation approach [2], and confirmed *ex situ* as ~7 nm. Thicknesses of the passive films are weakly potential dependent [3], in disagreement with the point defect model [4]. The *in situ* Raman experiments results indicated that the mixed oxide Cu_4O_3 plays a prominent role in the passive film [3]. Both *in situ* PL spectra and *in situ* ellipsometry spectra showed that the passive film of Cu is a defective phase. Passivity breakdown through OER was accompanied by the formation of singly charged oxygen vacancies with *in situ* PL. At the onset of strong defect-related PL, the thickness of the oxide layer decreased, which shows that breakdown of the oxide layer is triggered by defect formation [5]. *Ex situ* Hall effect measurements in collaboration with the Ruhr-Universität Bochum show that both passive oxide and transpassive oxide have n-type conductivity, in contrast to literature data [1]. Overall, a rather complex mechanism of dissolution results as illustrated in Fig. 1.

The effect of Cl^- on the properties of oxide film growing on Cu was studied using phosphate buffer saline (PBS, pH 7) [6]. Besides industrial relevance, Cu acts antibacterial. The corrosion mechanism of Cu in complex biological buffers is unknown. In PBS, corrosion products based on copper oxides, hydroxides, chlorides, phosphates, or mixed phases may develop. An early proposal for the corrosion mechanism of Cu in neutral Cl^--containing media assumed that the initial corrosion product is CuCl, which transforms into Cu_2O. In later works, copper oxide formation in Cl^--containing media was suggested to be a precipitation reaction rather than an electrochemical process. We observed that in PBS, the thickness of the growing film is dependent on the applied electrode potential. CuCl is only observed as a transient species before oxide formation. *Ex situ* surface analysis could not confirm the presence of CuCl (see Fig. 2). Cross sectional images show voids between the oxide layer and metal (Fig. 2). Inconsistencies became clear between *in situ* spectroscopy results and *ex situ* surface analysis. Based on observations and calculated predominance potential pH diagrams, the following model was proposed [6]. During anodic polarization, first Cu_2O forms. This film is rich in point defects, as suggested by its absorption spectrum, some of these are likely oxygen vacancies. These can be compensated by uptake of Cl^-, resulting in the first step in a chloride-rich, Cu_2O-based layer. As soon as the elec-

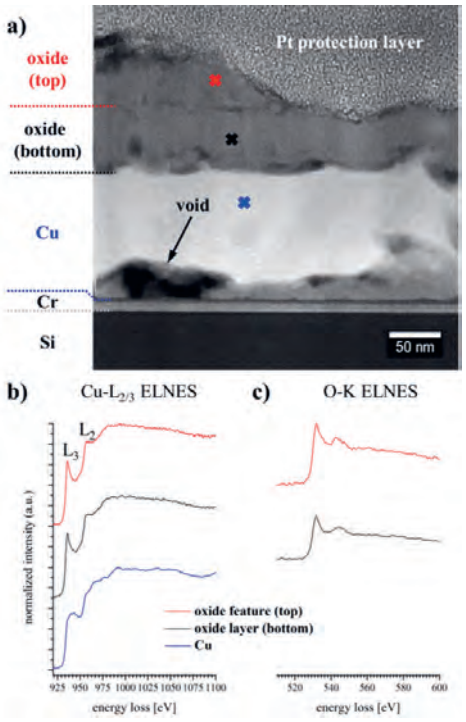

Fig. 2: *(a) Cross sectional scanning transmission electron micrograph shows the location where the presented energy electron loss spectra given in (b) and (c) were taken [6]. (b) Cu $L_{2/3}$ and (c) O K near-edge fine structures of the upper oxide feature (red), the lower oxide layer (black) and the Cu thin film (blue).*

trode potential increase triggers oxidation from Cu^{I} to Cu^{II}, the formation of soluble $CuCl_4^{2-}$ sets in, which may have precursors inside the film, or adsorbed to the surface. The dissolution of copper proceeds via chloride incorporation in oxygen vacancies in the defective Cu_2O [6]. As dissolution in the presence of biological material often proceeds at near neutral pH in an environment containing significant amounts of Cl^-, the results obtained in this work are relevant for the understanding of the surface electrochemistry of copper as antibacterial agent.

References

1. Schultze, J.W.; Hassel, A.W.: Encyclopedia of Electrochem 4 (2007) 216.
2. Chen, Y.; Erbe, A.: Surf Sci 607 (2013) 39.
3. Toparli, C.; Sarfraz, A.; Erbe, A.: Phys Chem Chem Phys 17 (2015) 31670.
4. Macdonald, D. D.: J Electrochem Soc 139 (1992) 3434.
5. Toparli, C. ; Sarfraz, A.; Wieck, A.D.; Rohwerder, M.; Erbe, A.: Electrochim Acta 236 (2017) 104.
6. Toparli, C.; Hieke, S. W.; Altin, A.; Kasian, O.; Scheu, C.; Erbe, A: J Electrochem Soc 164 (2017) H734.

Grain Boundary Phase States

A. Kwiatkowski da Silva [1], C. Liebscher [2], R. Hadian [3], B. Gault [1], D. Ponge [1], G. Dehm [2], J. Neugebauer [3], D. Raabe [1]

[1] Department of Microstructure Physics and Alloy Design (MA)
[2] Department of Structure and Nano-/ Micromechanics of Materials (SN)
[3] Department of Computational Materials Design (CM)

The local chemistry and structure of a grain boundary (GB) determines its energy, mobility, diffusivity, cohesive strength and sliding resistance, which directly affect the bulk materials' behaviour and properties such as impact toughness, creep resistance, fatigue, corrosion, and strength. GBs behave as quasi-two-dimensional phases, undergoing structural and chemical changes abruptly at critical values of thermodynamic parameters such as temperature, pressure and composition [1]. Recently, the term "complexion" was introduced to distinguish these equilibrium interfacial states from bulk phases [2]. GB phase states can be categorized by the type of transition that locally impacts GB properties through the formation of steps, facets or solute induced transitions of the GB core structure.

We have explored the impact of GB steps on GB mobility and discovered the atomistic mechanisms through molecular dynamics simulations. We found correlations between the type of steps that appear on the relaxed structure of a boundary and their migration energy barriers [3] as shown in Fig. 1. From this result we were able to conclude that the majority of general grain boundaries relax into steps with low symmetry, termed *kinked* boundaries which were shown to have the lowest migration barrier in comparison to flat and stepped boundaries. It was then observed that the facets in these *kinked* boundaries tend to coarsen in pure metals. This implies that general GBs dissociate into coarsely faceted segments, if faceting is not impeded or directed otherwise by alloying elements [4].

The generation and minimization of grain boundary structures is a precursor for migration simulations and we have designed an open access python package [5] that generates GB structures for atomistic simulations and additionally includes a minimization routine. Further *Jupyter* notebook scripts in the package give a step by step description on how to use the code to locate and produce GBs for *ab initio* or molecular dynamics simulations. It also serves as a platform to produce CSL properties for a given GB plane, such as CSL density.

Some of the extra functionalities of the code are as follows:

- Generation of different stepped structures
- Generation of large faceted structures
- Producing the displacement shift vectors (DSC) on a given GB plane. These vectors are conceptually considered to act as Burgers vectors of GB dislocations.

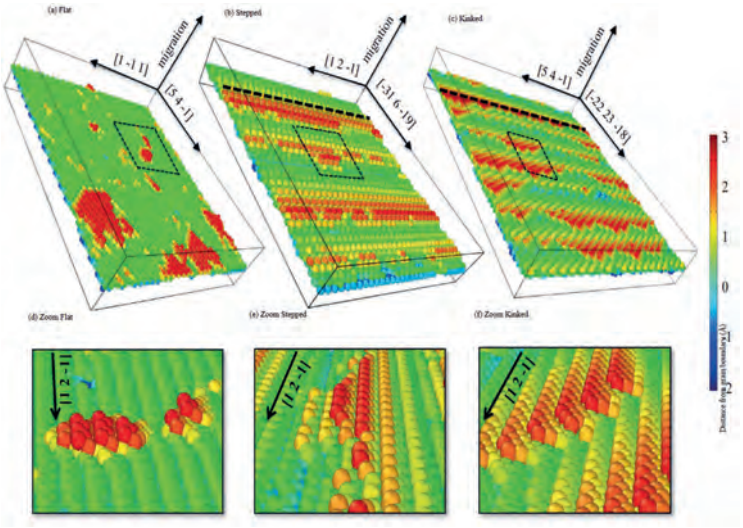

Fig. 1: *Migration mechanisms of flat (a), stepped (b) and kinked (c) grain boundaries. The colour code denotes height. Bulk atoms have been removed for clarity and only GB atoms are shown.*

The impact of phase transitions on the diffusivity or mobility of GBs has been intensively studied on idealized symmetric boundaries. In recent work, we could show that solute segregation is strongly anomalous in nanofaceted boundaries. In particular, the segregation of carbon (C) and iron (Fe) in multicrystalline silicon (Si) GBs is observed to occur at the facet junctions in contrast to the often assumed planar segregation at the facets themselves [6]. By using a combination of atomic resolution scanning transmission electron microscopy (STEM), atom probe tomography (APT) and molecular statics simulations, we were able to reveal that the atomic strain in the facet junctions dictates the segregation behaviour. Furthermore, we have systematically investigated the solute induced nanofaceting in asymmetric tilt grain boundaries. We could show that an initially flat, asymmetric copper (Cu) tilt GB develops silver (Ag) rich, nanometre sized facets upon controlled segregation as illustrated in Fig. 2 [7]. In combination with hybrid molecular dynamics and Monte Carlo simulations we established that this nanoscale GB phase transition is a result of a cascade of phase transitions and the

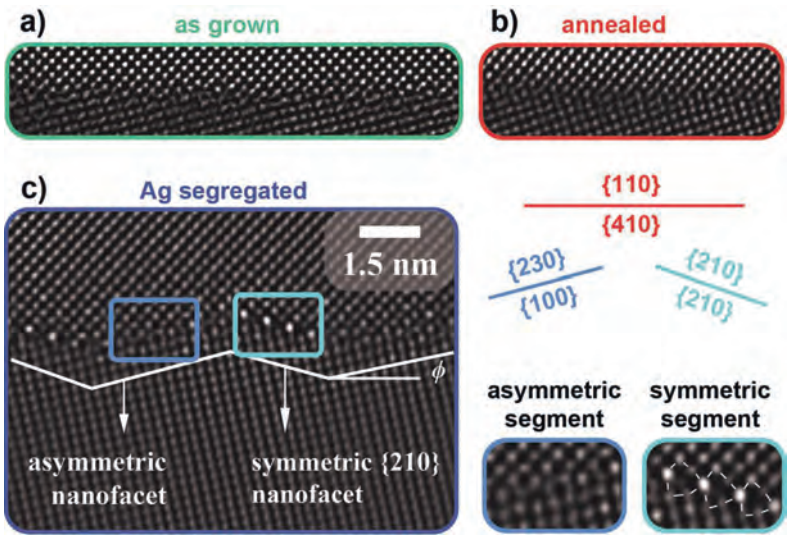

Fig. 2: *(a) Atomic structure of the asymmetric [001] Cu tilt grain boundary in the as grown state. (b) After annealing at 800ºC for 120 h. (c) Nanofaceted boundary after controlled Ag segregation annealed at 800ºC for 120 h.*

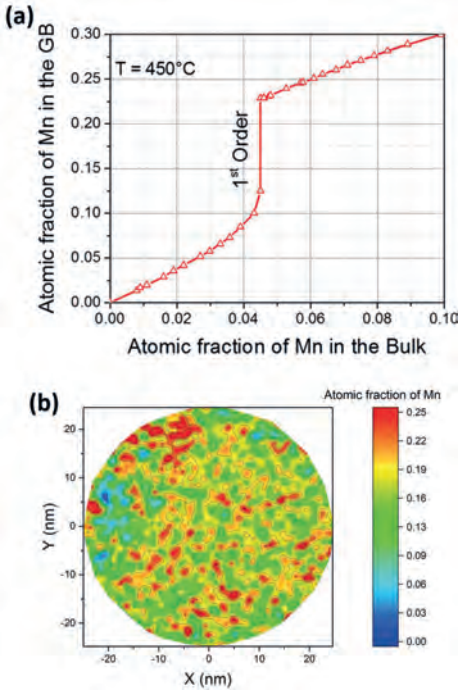

Fig. 3: *(a) Segregation isotherm at 450°C assuming metastable local equilibrium between the bulk and the grain boundary in a Fe-Mn BCC alloy. (b) 2D in-plane compositional analysis inside the grain boundary plane obtained by APT for a grain boundary from Fe-9 atomic % Mn solid solution, 50% cold-rolled, and annealed at 450 °C for 6 h.*

symmetric kite structure, shown in Fig. 2 c, is formed, due to its ability in taking up the highest amount of Ag atoms.

For solid-solid phase transformations, GB segregation is widely regarded as a pathway for phase transitions, since segregation to defects locally alters the thermodynamic driving force for phase nucleation by changing the chemical composition of the interfacial region. We developed an approach in order to quantitatively and qualitatively describe the Mn segregation in the BCC structure in Fe-Mn alloys which we systematically studied by Atom Probe Tomography (APT). This approach couples thermodynamic data from Calphad with a mean-field description of the grain boundary character what allows a more precise description of the segregation behaviour observed by APT than the more typical Langmuir-McLean segregation model [8]. The most important consequence of this model is that the presence of a spinodal region for the Fe-Mn BCC free-energy will lead to a first order transition of the grain boundary interface before the nucleation of austenite. This first order transition is typically represented in equilibrium segregation calculations as a discontinuous jump in the composition of the GB in function of the bulk composition (Fig. 3a). From a kinetics perspective, it implies the formation of metastable spinodal fluctuations (Fig. 3b) that tend to grow further with time at the segregated region, as observed by APT [4]. On the one hand, this increase in Mn content at the GB leads to an increase of the overall enthalpy of the boundary at lower temperatures and thus to embrittlement. On the other hand, these low-dimensional spinodal fluctuations on the GB act as precursor states to the nucleation of austenite when they become strong enough in composition amplitude and wavelength. Once austenite is formed, the amount of Mn segregated to the grain boundaries is drastically reduced and the toughness of the grain boundary is increased [9].

References

1. Dillon, S.J.; Tang, M.; Carter, W.C.; Harmer, M.P.: Acta Mater 55 (2007) 6208.
2. Tang, M.; Carter, W.C.; Cannon, R.M.: Phys Rev Lett 97 (2006) 0755021.
3. Hadian, R.; Grabowski, B.; Race, C.; Neugebauer, J.: Phys Rev B 94 (2016) 165413.
4. Hadian, R.; Grabowski, B.; Finnis, M.; Neugebauer, J.: Phys Rev Mat 2 (2018) 043601.
5. Hadian, R.; Grabowski, B.; Neugebauer, J.: The Journal Of Open Source Software 3 (2018) 900.
6. Liebscher, C.H.; Stoffers, A.; Alam, M.; Lymperakis, L.; Cojocaru-Mirédin, O.; Gault, B.; Neugebauer, J.; Dehm, G.; Scheu, C.; Raabe, D. : Phys Rev Lett 121 (2018) 015702.
7. Peter, N.J.; Frolov, T.; Duarte M.J.; Hadian, R.; Ophus, C.; Kirchlechner, C.; Liebscher, C.H.; Dehm, G.: Phys Rev Lett 121 (2018) 255502.
8. Kwiatkowski da Silva, A.; Kamachali, R.D.; Ponge, D.; Gault, B.; Neugebauer, J.; Raabe, D.: Acta Mater (2018) submitted.
9. Kwiatkowski da Silva, A.; Ponge, D.; Peng, Z.; Inden, G.; Lu, Y.; Breen, A.; Gault, B.; Raabe, D.: Nat Commun 9 (2018) 1137.

Dislocation Interactions with Twin Boundaries

C. Kirchlechner [1], N.V. Malyar [1], M.K. Kini [1], W.S. Choi [2], S. Sandlöbes [2], R. Hadian [3], B. Grabowski [3]

[1] Department of Structure and Nano-/ Micromechanics of Materials (SN)
[2] Department of Microstructure Physics and Alloy Design (MA)
[3] Department of Computational Materials Design (CM)

Coherent Σ3 twin boundaries are certainly one of the most prominent interfaces in structural materials. Firstly, because they can be introduced by numerous processes like crystal growth, annealing, or even cold working. Secondly, because they simultaneously allow for an extraordinary high strength while maintaining an outstanding ductility, two properties which are classically mutually excluding themselves but are combined in bulk nano-twinned materials [1]. The combination of high strength and ductility is the "holy grail" in structural materials and renders damage tolerance. The fundamental origin of the damage tolerance is, however, still not understood and currently studied across several departments of the MPIE.

We are focusing on the behaviour of single dislocations at twin boundaries and their mutual interactions. Dislocations can transmit through a twin boundary in two ways: (i) the "ideal" or also "soft" mode, where the Burgers vector of the dislocation is a shared lattice vector in both twin-grains. And, (ii), the "hard" mode, where the Burgers vector of the dislocation is not a low indexed lattice vector in the second grain, which complicates slip transmission considerably. During the last years we have developed and applied a complementary toolbox [2] of *in situ* scanning electron microscopy (SEM), *in situ* Laue microdiffraction (μLaue), transmission electron microscopy (TEM) as well as atomistic simulations to unravel and quantify the mechanisms of slip transmission through grain and twin boundaries.

The *in situ* SEM experiments are well suited for monitoring collective slip transmission processes in terms of slip trace analysis (see Fig. 1). This technique is well established and enables to study large sample numbers, often exceeding 100 samples per study. Recently, we were able to measure the activation volume and strain rate sensitivity of ideal slip transmission of dislocations through a coherent Σ3(111) twin boundary in copper [3]. The results point towards a cross-slip like dislocation transmission mode with a strain rate sensitivity of the twinned bicrystals similar to the single crystal.

Complementary to our SEM work, the μLaue technique can quantify the collective dislocation storage in terms of geometrically necessary dislocations in the grain interior and at the twin boundary. Furthermore, the local deviatoric strain tensor and crystallographic orientation can be measured. Using the ability of μLaue to measure the local orientation and number of dislocations in a pile-up, we were able to identify the stress required for ideal dislocation slip transmission through a coherent Σ3(111) copper twin boundary for the first time [4]. Surprisingly, this slip transmission stress (17 MPa) agrees well with the stress required for dislocation cross-slip in copper at the same temperature. Our results indicate that in at least three out of 12 slip systems copper twin boundaries do not act as strong barriers for dislocation slip. This might be extremely important during the local stress relaxation at crack tips in bulk nano-twinned materials. The extraordinary strength of these systems might

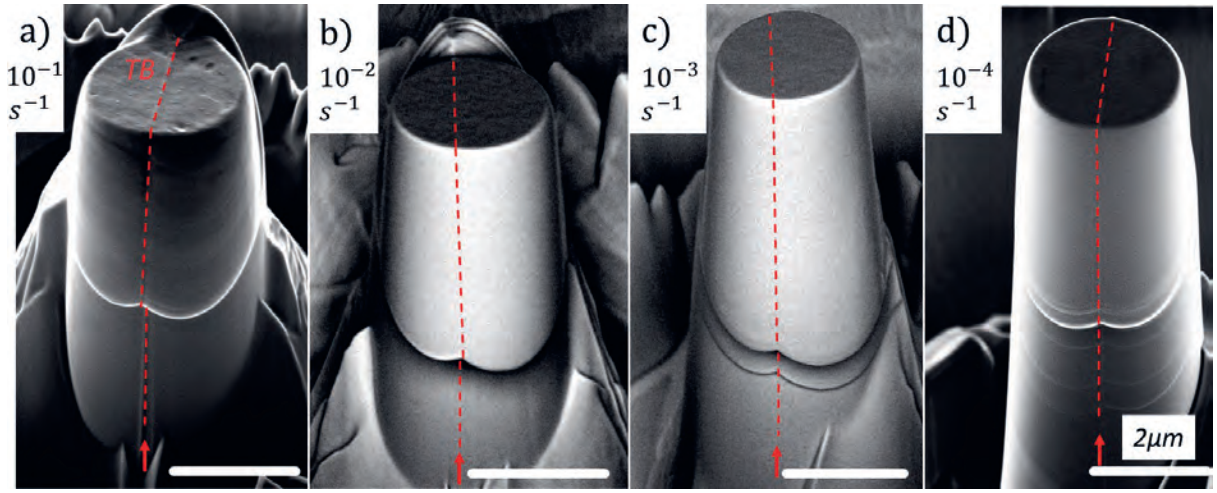

Fig. 1: *Micropillars deformed inside the SEM at different strain rates. The slip plane sharply kinks off at the location of the twin boundary. No significant differences in the activation of major slip steps can be identified.*

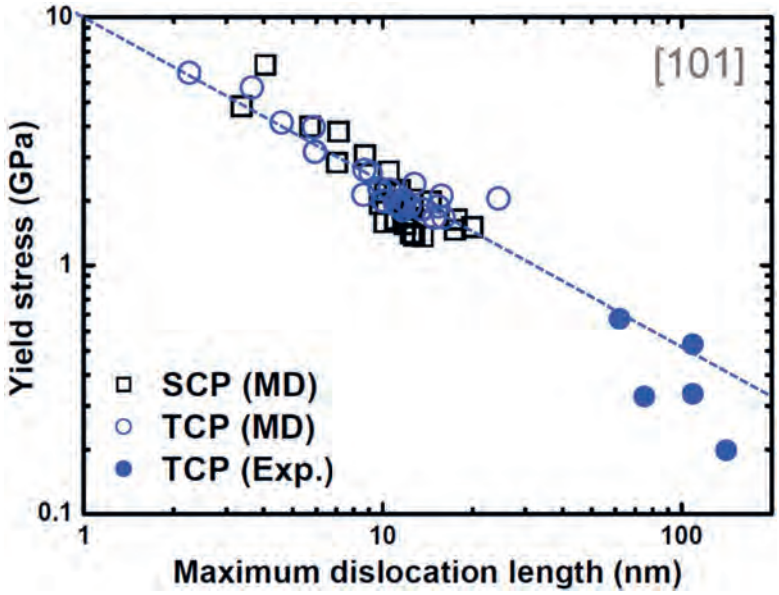

Fig. 2: *Correlation between the maximum dislocation length and the yield stress obtained from MD simulations for 42 nm sized nanopillars (open symbols) in comparison with experimental data from Imrich et al. [9]. SCP refers to single crystalline pillars and TCP to twin crystalline pillars. The extrapolation (blue dotted line) is based on a power fitting function and uses as input only the MD data for twin crystal pillars (blue empty points). The agreement with experiment is excellent.*

however be caused by compatibility requirements, which is currently investigated on nano-twinned silver thin films with twin thicknesses ranging from 10 nm to 1 µm.

In situ and *post mortem* TEM analysis are an ideal tool to understand the interactions of single dislocations with twin boundaries, as well as the impact of local chemistry on dislocation mobility. We have applied TEM not only on Σ3(111) boundaries in copper, but have also quantified the importance of twinning, double-twinning and slip transmission on the mechanical properties of Fe-Mn-C twinning-induced plasticity steel (TWIPs) [5,6].

The three experimental tools are finally complemented by MD simulations which shed light on possible mechanisms active during slip transfer [7, 8]. Our current work thereby focuses on the importance of the initial dislocation structure on the slip transmission properties [8]. For this purpose we have deformed pristine pillars requiring stresses close to the theoretical shear stress of copper for plastic deformation. Furthermore, we used high vacancy concentrations and subsequent thermal annealing to produce a natural dislocation network in our MD pillars (see Fig. 2). These pillars deformed at significantly lower stresses than the pristine ones. Also, the micropillars with a grown-in dislocation network exhibit slightly higher yield stresses than their single crystalline counter parts with similar dislocation structures. Snapshots taken during slip transmission point towards a double-hump like dislocation transfer mechanism which supports the experimental observations from SEM and µLaue on strain rate sensitivity and transmission stress.

References

1. Lu, K.; Lu, L.; Suresh, S.: Science 324 (2009) 349.
2. Dehm, G.; Jaya, B.N.; Raghavan, R.; Kirchlechner, C.: Acta Mater 142 (2018) 34.
3. Malyar, N.V.; Grabowski, B.; Dehm, G.; Kirchlechner, C.: Acta Mater 161 (2018) 412.
4. Malyar, N.V.; Micha, J.S.; Dehm, G.; Kirchlechner, C.: Acta Mater 129 (2017) 91.
5. Choi, W.S.; Sandlöbes, S.; Malyar, N.V.; Kirchlechner, C.; Korte-Kerzel, S.; Dehm, G.; De Cooman, B.C.; Raabe, D.: Acta Mater 132 (2017) 162.
6. Choi, W.S.; Sandlöbes, S.; Malyar, N.V.; Kirchlechner, C.; Korte-Kerzel, S.; Dehm, G.; Choi, P.-P.; Raabe, D.: Scr Mater 156 (2018) 27.
7. Jeon, J.B.; Dehm, G.: Scr. Mater 102 (2015) 71.
8. Ko, W.S.; Hadian, S.; Nematollahi, G.A.; Jeon, J.B.; Dehm, G.; Neugebauer, J.; Kirchlechner, C.; Grabowski, B.: Acta Mater (2019) in preparation.
9. Imrich, P.J.; Kirchlechner, C.; Kiener, D.; Dehm, G.: Scr Mater 100 (2015) 94.

Local Chemistry at Planar Defects in Off-stoichiometric Binary Alloys

C. Liebscher [1], F. Stein [1], M. Slapakova [1], A. Zendegani [2], T. Hickel [2], J. Neugebauer [2], D. Palanisamy [3], D. Raabe [3], B. Gault [3]

[1] Department of Structure and Nano-/ Micromechanics of Materials (SN)
[2] Department of Computational Materials Design (CM)
[3] Department of Microstructure Physics and Alloy Design (MA)

Properties of materials are to a wide extent determined by the presence of defects. They may be either artificially introduced into the material or can be intrinsic defects. The stability and concentration of these defects is closely related to their atomic structure, which can already be complex for planar defects in pure elements or chemically ordered phases, such as Laves or Heusler alloys. In the case of multi-component alloys with off-stoichiometric compositions, the chemical degree of freedom adds another level of complexity. The excess atoms can form point defects (antisite atoms or vacancies) and can be accommodated by extended defects. Already a segregation of individual atoms yields an additional stabilization of these defects. Particularly fascinating becomes the interplay of local chemistry and planar defects, however, if defect structures and/or compositions are created that would not be present otherwise.

In the present article, we highlight two examples of binary intermetallic alloys that show such phenomena: First, we have observed novel atomic structures connected to planar stacking faults in phase-pure samples of the hexagonal Laves phase $NbFe_2$. They substantially change their concentration and therewith the mechanical performance of a phase, which is important for precipitation hardening in high-temperature steels [1-3]. Second, we have detected an unusual enrichment of Mn at twin boundaries in the binary $Al_{45}Mn_{55}$ Heusler alloy (τ-phase). These extended defects contribute to magnetic domain wall nucleation or act as pinning sites and are thus important for the magnetic response of a material, which is a potential low-cost replacement of medium performance ferrite-based magnets.

The significant increase in the defect density of the Laves phase $NbFe_2$ was observed with scanning transmission electron microscopy (STEM) in samples with 35 at.% Nb, while stoichiometric samples (33 at.% Nb) showed only isolated dislocations. Besides antisite occupation, various types of planar faults appear. We observed numerous extended planar defects parallel to the basal plane of the hexagonal structure, introducing Nb-enriched layers of various thicknesses, as well as a high number of confined basal and pyramidal planar faults. All types of observed basal and pyramidal faults contain structural motifs, which are characteristic for the crystal structure of the μ phase Nb_6Fe_7 (46 at.% Nb) in the same binary system. Interestingly, however, the

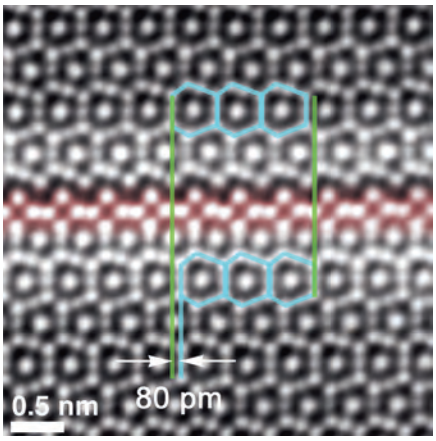

Fig. 1a: *Atomic resolution low angle annular dark-field (LAADF) STEM image of a basal fault in a Nb-rich $NbFe_2$ Laves phase with μ phase type building blocks. The shift of the upper and lower part and the single three-layer stack of the slab are highlighted.*

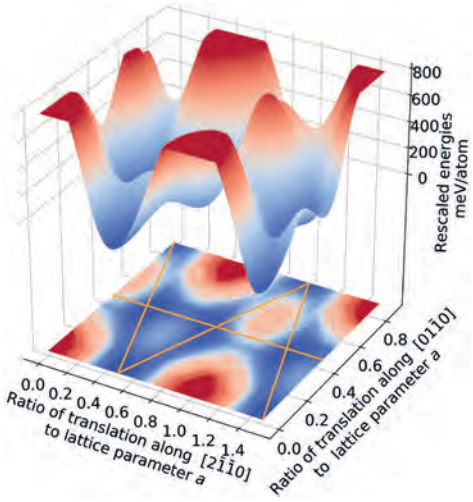

Fig. 1b: *The basal generalized stacking fault energy surface (γ surface) of the two half crystals in the STEM image. All structures along the orange lines reproduce in one projection the STEM image.*

stacking of the μ phase is not fulfilled in the atomic layers next to the defects, despite the increased Nb content. One of the variations in the stacking sequence is the omission of an Fe-layer, so-called Kagome layer, as shown in Fig. 1a.

We used *ab initio* calculations to determine the formation energies of these planar defects. A prerequisite was to find the exact crystallographic structure underlying the experimental STEM images, since the restriction to a single projection is still consistent

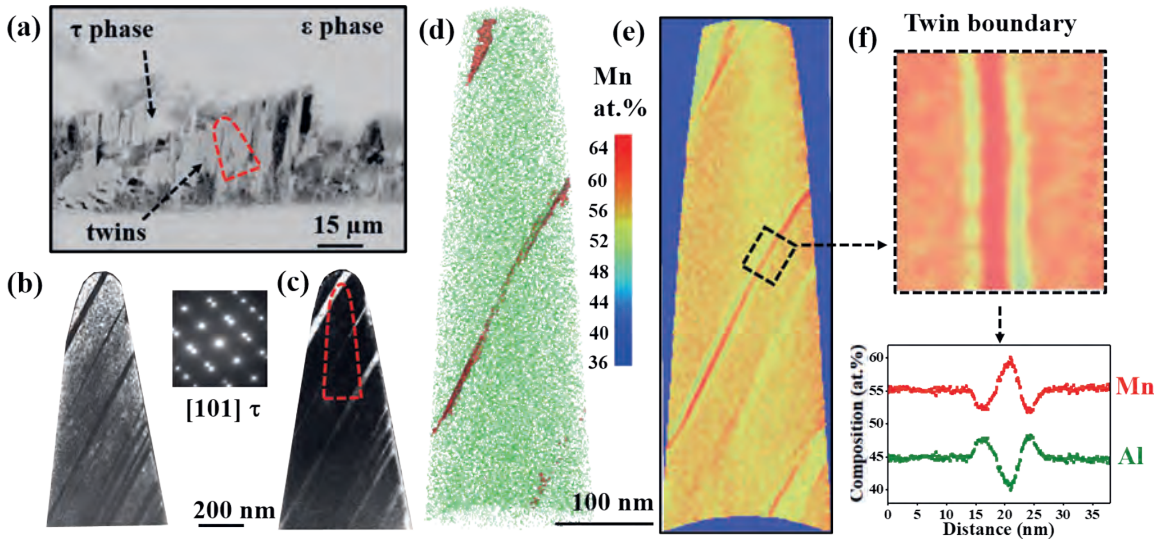

Fig. 2: *(a) Back-scattered electron SEM image of the $Al_{45}Mn_{55}$ ε phase sample annealed at 450 °C for 15 minutes showing massive growth of τ phase on ε phase grain boundaries. The red triangle is the location from where the atom probe tips have been extracted. (b) Bright field (BF) image taken near to [101] τ phase zone axis. (c) Dark field (DF) image taken from the twinning spot. (d) Atom probe reconstruction showing distribution of Al atoms (green colour) and iso-compositional interfaces with 60 at.% Mn (red colour) showing Mn enrichment confined to twins. (e) 2D composition plot with colour scale for Mn at.% across the APT tip reconstruction projected to the plane perpendicular to the viewing direction. (f) 2D and 1D composition plots showing Mn enrichment along the twin boundary.*

with multiple translational variants perpendicular to the image plane. Therefore, the generalized stacking fault energy (SFE) surface was determined by *ab initio* calculations (Fig. 1b). The energy of the most stable crystallographic Nb-enriched defect structures was then compared with a phase separation of the off-stoichiometric composition into a perfect Laves and a perfect μ phase. While the defects turned out to be not stable in equilibrium conditions, some of them become energetically favourable as compared to a phase separation that involves a laterally strained μ phase. This explains why a nanoprecipitation of μ phase is less likely than the observed extended defects.

The second example, $Al_{45}Mn_{55}$, is a metastable intermetallic phase with a $L1_0$ ordered structure. This compound, denoted as 'τ', evolves by suppressing the formation of equilibrium β-Mn (cubic) and γ_2 (Al_8Mn_5, rhombohedral) phases from the high temperature hexagonal-close packed ε phase and has a strong uniaxial magneto crystalline anisotropy. The microstructural development in the alloy takes place through massive mode and a large number density of defects such as twins, stacking faults and antiphase boundaries appear during the thermal history of the material [4]. Our combined electron microscopy and atom probe tomography approach revealed the structure and composition of some defects [5], as shown in Fig. 2. The extraordinary observation in this case, is the enrichment of twin boundaries by approx. ~8 at.% Mn with a confined depletion outside the boundaries. This evidences an occurrence of a short-range solute diffusion during the ε→τ-phase transformation. A more detailed study involving *ab initio* calculations is underway, and we aim to better understand the driving forces of this segregation behaviour and its effect to the defects on the magnetic properties for the $Al_{45}Mn_{55}$ alloy. This approach is also expanded to low rare earth containing high performance magnets such as Sm-Fe-Ti based, in collaboration with Professor Oliver Gutfleisch's Functional Materials group in TU Darmstadt. The obtained results and their interpretation will be used for improving the magnetic properties of these alloys by means of further tuning alloying and processing.

References

1. Šlapáková, M.; Liebscher, C.; Kumar, S.; Stein, F.: Proc Intermetallics (2017) 50.
2. Šlapáková, M.; Kumar, S.; Liebscher, C.; Zendegani, A.; Hickel, T.; Neugebauer, J.; Stein, F.: *in preparation* (2018).
3. Zendegani, A.; Šlapáková, M.; Liebscher, C.; Stein, F.; Ladines, A.N.; Hammerschmidt, T.; Drautz, R.; Körmann, F.; Hickel, T.; Neugebauer, J.: Proc. Intermetallics (2017) 89.
4. Palanisamy, D.; Singh, S.; Srivastava, C.; Madras, G.; Chattopadhyay, K.: Metall Mater Trans A47 (2016) 6555.
5. Palanisamy, D.; Raabe, D.; Gault, B.: Scr Mater 155 (2018) 144.

Tribology of Steels

S. Brinckmann [1], M. Herbig [2]

[1] Department of Structure and Nano-/ Micromechanics of Materials (SN)
[2] Department of Microstructure Physics and Alloy Design (MA)

Friction of sliding components and surface wear occur in the majority of transportation and manufacturing systems. The associated friction induced energy losses are high, in combustion engines they are around 30-40%. Steels are often used for these applications as they offer low friction surfaces with ultra-mild wear volumes (<1×10^{-7} mm^3 per periodic cycle). Steel contacts can be either unlubricated (e.g. in the food industry) or lubricated to further reduce friction and wear.

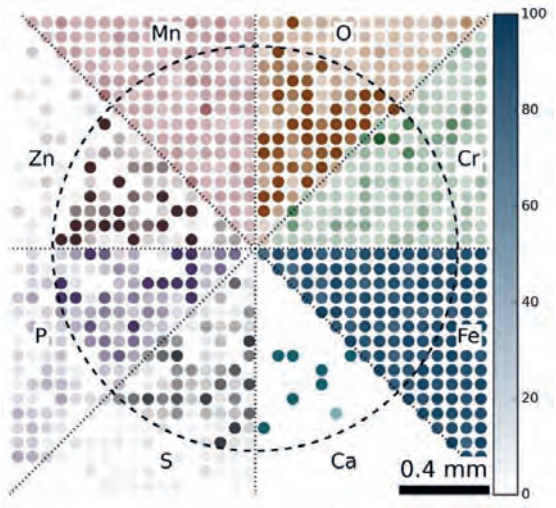

Fig. 1: *Distribution of elements in the macroscale cyclic contact as determined by quantitative electron probe microanalysis EPMA. The maxima are 100at.% for Fe; 5at.% for Cr, O; 1at.% for Mn; 0.5at.% for Zn;0.2at.% for P, S; 0.02at.% for Ca. The experiment was carried out using 100Cr6 steel on steel contact with ZDDP in a mineral oil.*

Lubricants use a number of additives that improve the wear resistance and reduce friction. Zinc-dialkyldithiophosphates (ZDDP) are currently the most frequently used anti-wear additives, which result in roughly 100 nm thin and amorphous surface layers that consist of material patches that have a few micrometer extension. However, improved environmental standards require a decrease in the use of phosphates and sulphates. To mirror the beneficial behaviour of ZDDPs onto next generation additives, the generation mechanisms of ZDDP-induced tribolayers have to be identified. To this end, we - in collaboration with colleagues at the Institute for Machine Elements and Systems Engineering, RWTH Aachen University - investigated the tribofilm generation by focusing on the mechanical activation of surface layer growth (Fig. 1).

We executed cyclic contact experiments (90 k cycles; 1.89 MPa contact pressure; frequency 2.5 Hz at macroscale and 0.33 Hz at microscale) at the macroscale (sphere radius = 27 mm) and microscale (sphere radius = 145 µm) and quantified the surface chemistry. The observed films are chemically and topographically similar to layers that evolve during conventional tribology [1]. In these layers, Zn, P and S are enriched compared to the contact outside and more oxygen is present. Moreover, the size of the film is similar to the Hertzian contact domain. This knowledge will be used to create a tribolayer growth model.

In addition to chemical surface layers, also the subsurface microstructure evolves during tribological loading. We studied the deformation of an austenitic [2,3] and pearlitic steel during microasperity friction. In pearlite, we observed that the cementite lamellae deform by bending (Fig. 2), undergo severe thickness changes and shear while only few lamellae fracture; despite of the brittle nature of cementite. The understanding of the ductile behaviour of cementite during microtribology requires a fundamental understanding of the local deformation. To this end, we executed microcantilever bending and micropillar compression experiments of pure cementite samples. Those experiments revealed that dislocation-mediated plasticity occurs as discete slip steps are present on the cantilever and pillar surface. The maximum plastic strain is on the order of 7% in pillar compression. However, the microscale experiments failed to exhibit severe bending as observed during microtribology. To further the insight of the severe bending, FEM simulations were executed to quantify the adiabatic heating due to plastic deformation. Those simulations revealed temperatures in excess of 600°C during microtribology.

The above described activities on pearlite target basic tribological principles and prepare the ground for understanding a complex phenomenon occurring during service in bearings: the formation of white etching cracks (WECs). These initiate below the bearing surface and eventually extend to the raceway what leads to catastrophic failure. Although this failure mode is known for more than 100 years and causes enormous economic costs worldwide so far neither the mechanism is understood nor are reliable countermeasures available. The research activities at the MPIE have revealed that failure by WEC is caused by a so far unknown crack propa-

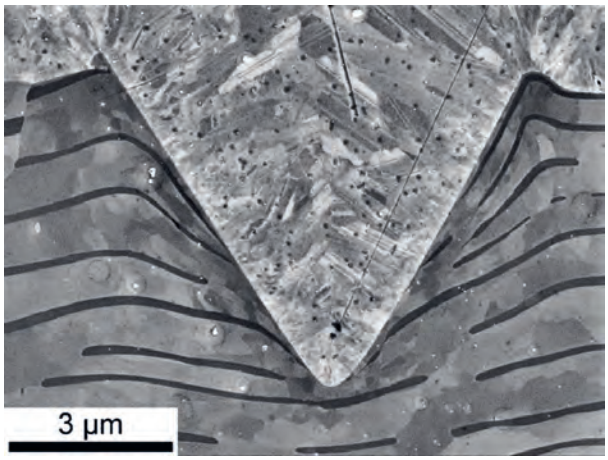

Fig. 2: *Cross-section of pearlite after microtribological experiment: cementite lamellae being embedded in ferrite can be deformed plastically although cementite on its own has only little ductility. The sample was enclosed by Ni for protection during cross-section preparation.*

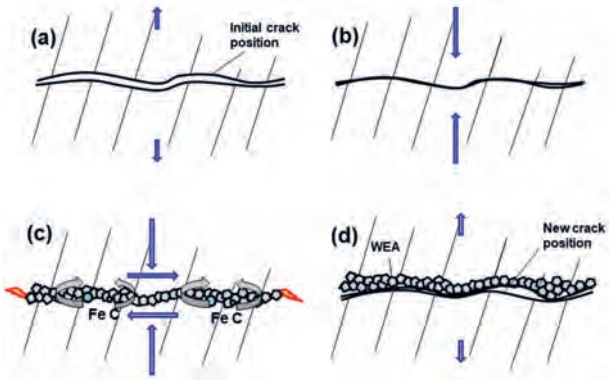

Fig. 3: *White etching crack (WEC) and white etching area (WEA) formation mechanism. During compressive loading cycles fracture surface rubbing occurs, leading to material transport between the fracture surfaces what causes a macroscopic change of the crack position.*

gation mechanism [4]. Cracks have been known to continuously extend until failure occurs and this holds also for WECs. However, WECs show additionally to that a unique particularity: they "roam" through the material, viz. they continuously change their position, leaving behind a severely plastically deformed area. This so called white etching area (WEA) consist of nanocrystalline ferrite surrounded by carbon (C) grain boundary segregation [5] as known also from the case of cold drawn pearlitic wires.

As WECs initiate within the bulk, their fracture surfaces are not oxidized. When these get in contact during a compressive loading cycle strong adhesive forces form and material can be transferred from one side of the fracture surface to the other. Many repetitive loading cycles lead to a macroscopic change in the crack position (Fig. 3). The element C plays a key role in the process [6] as it - on the one hand - stabilizes the WEA microstructure by lowering the grain boundary energy, whichreduces the driving force for dynamic recrystallization [5]. On the other hand, C forms a film on the fracture surfaces which prevents the complete closure of the crack and supposedly acts as a solid lubricant that facilitates fracture surface rubbing.

The formation of WECs involves the decomposition of carbides which act as a reservoir for C. Further research is targeted towards understanding precipitate stability and decomposition. The remarkable immunity of high nitrogen (N) bearing steels to WEC failure is elucidated by systematic comparison to the commonly employed high C bearing steels. Further, the influence of electric current in combination with deformation on the decomposition of cementite is currently being investigated. In future, tribological tests drawing cementite over ferrite will give insights into the processes occurring during WEC fracture surface rubbing. As the dislocation velocity influences solute drag, the influence of the deformation rate on cementite decomposition will be investigated using a custom-built rolling contact fatigue device. Further, the influence on hydrogen (H) on cementite decomposition will be investigated with a modified nanoindenter that allows *in situ* H charging.

References

1. Brinckmann, S.; Stratmann, A.; Dehm, G.; Jacobs, G.: Tribol Int 129 (2019) 436.
2. Brinckmann, S.; Dehm, G.: Wear 338 (2015) 436.
3. Brinckmann, S.; Fink, C.A.C.; Dehm G.: Wear 338 (2015) 430.
4. Morsdorf, L.; Mayweg, D.; Diederichs, A.; Li, Y.; Mayer, J.; Raabe, D.; Herbig, M.: Acta Mater (2018) in preparation.
5. Li, Y.J.; Herbig, M.; Goto, S.; Raabe, D.: Mater Charact 123 (2017) 349.
6. Mayweg D.; Morsdorf, L.; Raabe, D.; Herbig, M.: Acta Mater (2018) in preparation.

Hydrogen Effect on the Mechanical Properties of Metallic Materials

S. Brinckmann [1], J. Duarte [1], M. Rohwerder [2], H. Luo [2], Z. Li [3], D. Ponge [3], T. Hickel [4]

[1] Department of Structure and Nano-/ Micromechanics of Materials (SN)
[2] Department of Interface Chemistry and Surface Engineering (GO)
[3] Department of Microstructure Physics and Alloy Design (MA)
[4] Department of Computational Materials Design (CM)

Experiments on hydrogen trapping sites: The increasing use of high strength steels, Ni base superalloys and aluminium alloys led to a renewed interest in understanding H uptake and trapping in metallic materials. The strength of trapping and diffusivity of H depends on the microstructure. This investigation requires suitable methods for H detection. The Scanning Kelvin Probe Force Microscopy (SKPFM) is a high lateral resolution, unprecedented sensitivity technique for H detection that was applied for a number of different materials, e.g. Pd, Fe, duplex steel and Ni-Nb alloys [1-4]. The trapping sites inside a Fe-5 wt.-% Ni model alloy were characterized using a combination of Thermal Desorption Spectroscopy (TDS) and SKPFM (see Fig. 1*)*. The TDS detects no traps in the recrystallized material, but indicates at least two traps in the cold rolled material. They were identified as dislocations and vacancies with desorption energies of 29 and 38 kJ/mol (0.3eV and 0.39eV) [5]. The SKPFM and Kelvin Probe (KP) measurements give indirect confirmation that the vacancy density is higher close to inclusions, most probably at the oxide inclusion-matrix interface, and that even the recrystallized material has such H traps. In Fig. 1b), KP allows obtaining quantifiable potentials and shows that the average background signal is much higher for the cold rolled sample compared to the recrystallized one, indicating a 100 times higher H release rate. This means that the H release around inclusions detected by SKPFM is much lower in the recrystallized sample than in the cold rolled one. This example shows the advantage of using a combination of TDS and SKPFM for a more detailed trap characterization of materials.

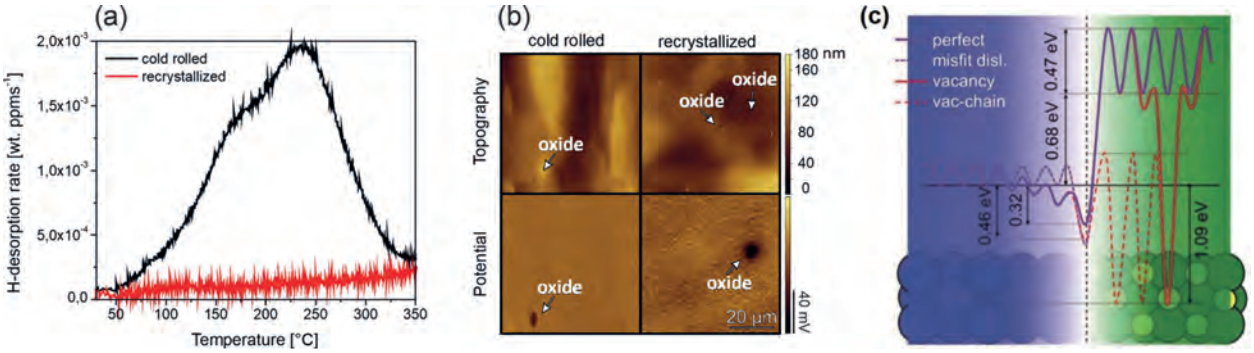

Fig. 1: *(a) TDS and (b) SKPFM map for a Fe-5 wt.% Ni alloy [5]. (c) Energy profiles of H at a (001)Fe/(001)TiC interface, which is perfect (purple solid), contains a misfit dislocation (purple dashed), a vacancy in the carbide (red solid), or a chain of vacancies starting at the interface (red dashed), see also [6].*

Simulations on hydrogen trapping sites: *Ab initio* based simulations allow us a systematic study of the H trapping next to precipitates and inclusions, taking the impact of vacancies as well as the possibility of H-enhanced decohesion into account. Investigations have, for example, been performed for cementite, k carbide, Cr carbides, and TiC, in the CM department and in collaboration with external groups. In the prototype case of TiC precipitates misfit dislocations and incoherencies have been simulated by well-defined crystal translations and modified orientation relationships, respectively [6]. The good agreement with trapping energies measured in TDS validates the reliability of this approach. We observe that the trapping of H to a perfectly coherent interface is moderate (0.32 eV) and is slightly enhanced (0.46 eV) for misfit dislocations (Fig. 1c). There are different scenarios for the trapping by C vacancies near the interface. Directly at the interface, a C vacancy yields a similar trapping energy as for misfit dislocations, while a vacancy insight the carbide shows a very deep trap with barriers of more than 1.7 eV. The most efficient trapping mechanism are chains and accumulations of C vacancies near the TiC interface to the matrix, a scenario that could explain the large traps at oxide-matrix interfaces, as measured by SKPFM and TDS.

Influence of hydrogen on incipient plasticity in iron alloys: The failure mechanisms that initiate at the atomic scale due to H absorption and interaction with trap binding sites, i.e. interfaces, precipitates or dislocations, can be studied independently by nanoindentation due to the small volume probed. In addition, *in situ* charging the sample with H avoids the formation of concentration gradients related to desorption. Two custom electrochemical cells were

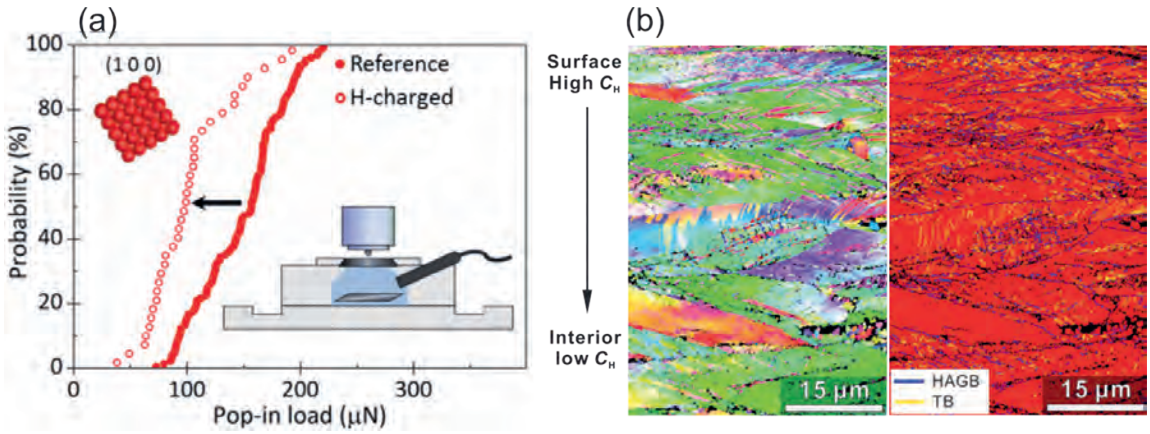

Fig. 2: *(a) Cumulative plot of the pop-in load for the (1 0 0) grain orientation showing a decrease related to H charging. Inset: back-side set-up for electrochemical charging. (b) Nanotwinned microstructure in a high entropy alloy with a high H concentration at the surface (top side) and low H concentration in the interior (bottom side). Inverse pole figure map of the grain orientation determined by electron backscatter diffraction (EBSD).*

built for *in situ* H charging during nanoindentation: "front-side" charging with the sample and indenter tip immersed into the electrolyte, and "back-side" charging where the analyzed region is never in contact with the solution. As case study, we investigate homogeneous nucleation of dislocations in bcc FeCr alloys depending on the H content. While directly charging with H in the back-side setup (inset in Fig. 2a), KP measurements over a Fe-20 wt.%Cr alloy showed a fast H diffusion rate towards the upper surface ($1.5x10^{-6}$ cm^2/s) as well as a pronounced release flow. During nanoindentation, a reduction in the pop-in load indicating the yield stress decrease with the increase of H content. The formation of multiple pop-ins provides evidence for the decrease in the resolved shear stress and enhanced dislocations nucleation. This behaviour is consistent with a multiscale simulation of homogeneous dislocation nucleation combining atomistic information (e.g., dislocation-core structure, H-H interaction) and a self-consistent iterative method for the local H concentration in a dislocation stress field [7]. According to that approach, the reduced critical shear stress can be explained as an effective decrease of the dislocation line energy due to the interaction with diffusible H.

Hydrogen in CoCrFeMnNi High Entropy Alloy (HEA): Besides the conventional alloys discussed above, we also probed the H effects on the novel high-entropy alloys which contain multiple principal elements in equiatomic or near-equiatomic concentrations. We demonstrated that H can be utilized for the case of an equiatomic CoCrFeMnNi HEA to tune beneficial strengthening and toughening mechanisms rather than undergoing catastrophic failure due to H embrittlement at room temperature [8]. Specifically, our work showed that a proper concentration of H actually jointly increases both strength and ductility of the CoCrFeMnNi HEA. This stress and ductility increase is owing to the fact that H can cause a significant increase in the nano-twin density, thereby increasing the alloy's work-hardening capability, and thus increasing both strength and ductility [8]. We further investigated the H effect on the CoCrFeMnNi HEA at cryogenic temperatures. It was found that the exceptional damage tolerance of this HEA at cryogenic temperatures can be maintained even when exposed in H containing environment [9]. This resistance is enabled by a self-accommodation mechanism: the higher the local H content, the higher is the twin formation rate. Accordingly, the H's through thickness diffusion gradient translates into a nano-twin gradient that counteracts material weakening by enhanced local strengthening (Fig. 2b). The beneficial effect of the gradient nano-twin structure overcompensates the H embrittlement, and hence leading to the absence of H-induced surface cracks upon tensile deformation at cryogenic temperatures [9]. Thus, these investigations provide new insights for designing H tolerant materials.

References

1. Evers, S.; Rohwerder, M.: Electrochem Comm 24 (2012) 85.
2. Evers, S.; Senöz, C.; Rohwerder, M.: Sci Technol Adv Mat 14 (2013) 1.
3. Senöz, C.; Evers, S.; Stratmann, M.; Rohwerder, M.: Electrochem Comm 13 (2011) 1542.
4. Tarzimoghadam, Z.; Rohwerder, M.; Merzlikin, S.V.; Bashir, A.; Yedra, L.; Eswara, S.; Ponge, D.; Raabe, D.: Acta Mater 109 (2016) 69.
5. Krieger, W.; Merzlikin, S.V.; Bashir, A.; Szczepaniak, A.; Springer, H.; Rohwerder, M.: Acta Mater 144 (2018) 235.
6. Di Stefano, D.; Nazarov, R.; Hickel, T.; Neugebauer, J.; Mrovec, M.; Elsässer, C.: Phys Rev B 93 (2016) 184108.
7. Leyson, G.P.M.; Grabowski, B.; Neugebauer, J.: Acta Mater 107 (2016) 144.
8. Luo, H; Li, Z.; Raabe, D.: Sci Rep 7 (2017) 9892.
9. Luo, H.; Lu, W.; Fang X.; Ponge, D.; Li, Z.; Raabe, D.: Mater Today (2018) in press.

Nucleation and Growth of Stable Hydrides

Y. Chang [1], I. Mouton [1], W. Lu [2], A. Breen [1], S. Zhang [3], S. Wang [4], D. Vogel [5], A. Ackermann [4], D. Dye [4], T.B. Britton [4], C. Scheu [3], T. Hickel [6], C. Liebscher [2], M. Rohwerder [5], G. Dehm [2], D. Raabe [1], B. Gault [1]

[1] Department of Microstructure Physics and Alloy Design (MA)
[2] Department of Structure and Nano-/ Micromechanics of Materials (SN)
[3] Independent Max Planck Group on Nanoanalytics and Interfaces (NG)
[4] Department of Materials Science & Engineering, Imperial College London
[5] Department of Interface Chemistry and Surface Engineering (GO)
[6] Department of Computational Materials Design (CM)

Hydrogen embrittlement (HE) is a significant challenge in high strength alloys were the ingress of H can cause a sudden and often catastrophic loss in ductility and premature failure. Ti and Zr based alloys are both known to be particularly prone to HE. Direct quantification of H in alloys with near-atomic resolution is critical to gain a better understanding of HE and has only recently become a possibility through the use of advanced atom probe tomography (APT) techniques. Isotope marking with deuterium (D) allows to discriminate D from within the specimen from the spurious residual H from the vacuum chamber of the microscope. Both Ti and Zr, and their respective alloys have a high affinity for hydrogen and are typical hydride formers.

We charged a Zircaloy-4 with D to form stable deuterides and successfully characterised the nanostructure of the deuteride growth front using APT. We observed by a combination of transmission electron microscopy and atom probe tomography the presence of an intermediate, metastable deuteride present at the interface with the metal, as well as rejection of Sn from the deuteride, with a significant enrichment of Sn at the growth front of up to 2 at.%. This behaviour suggests that Sn may help to retard further deuteride growth and have a significant influence on the growth rate. Such information could have significant implications for controlling hydride evolution in Zr based alloys and reducing the severity of DHC [1].

In parallel, significant efforts have been devoted to investigating hydride formation in titanium. Ti-hydrides are brittle phases which cause premature failure of Ti-alloys. Ti adopts either a hexagonal close-packed structure, (α) which has negligible solubility for H, and a body-centred cubic structure, (β) which can absorb significant amounts of H. The main model for embrittlement involves the growth of hydride films at interfaces that provide rapid transport of H, enhance segregation and thus accelerate hydride nucleation and growth, where crack initiates and propagates. We revealed by joint transmission electron microscopy and atom probe tomography that hydrides are prone to form at α/β interfaces and/or α lath boundaries in both pure-Ti and an array of alloys. The example of Ti-4 wt.%Mo is summarised in Fig. 2 (a-f). In contrast, Al-containing commercial alloys, such as Ti-6Al-4V and Ti-6Al-2Sn-4Zr-6Mo alloys, could dissolve slightly more H and do not show hydrides. The strength of the α matrix seems to play

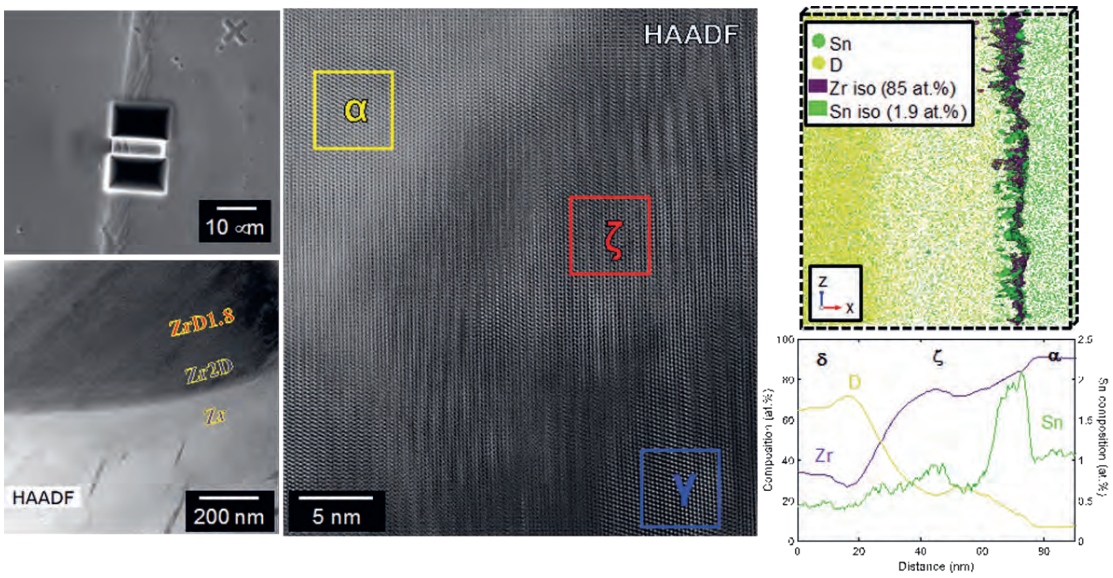

Fig. 1: *Focused-ion beam preparation of the specimen from a specific deuteride; conventional and high-resolution transmission electron microscopy of the deuteride-metal interface; Close-up on an atom probe tomography reconstruction and composition profile of the complex deuteride-metal interface.*

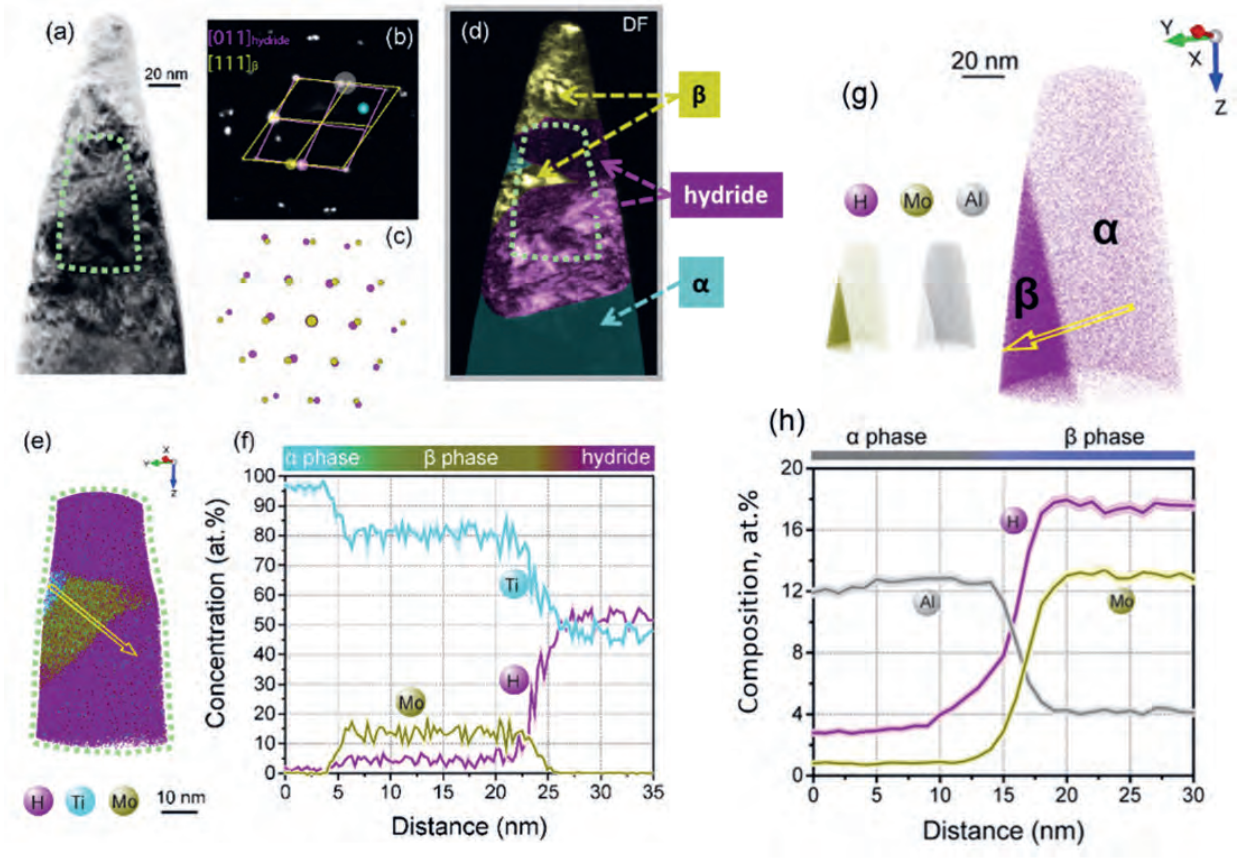

Fig. 2: *(a-f) Correlative TEM and APT analysis showing hydride formation at α/β interfaces in a Ti-4 wt.% Mo binary alloy; (g-h) H distribution and composition profile across the α/β interface in Ti-6Al-2Sn-4Zr-6Mo.*

a prominent role in hindering hydride formation, as the hydride growth must be accommodated by both elastic and plastic deformation. Therefore, the alloyed α phase probably requires greater supersaturation of H to create an adequate driving force for the formation of hydride. Our studies confirmed that Al alloying could increase H solubility in α and suppress hydride precipitation in Ti-alloys. The implication of our findings is that hydrogen embrittlement in commercial Ti alloys (with Al addition) near room temperature is probably not a consequence of hydride formation but the concentration of H in the β phase that can promote local decohesion or enable enhanced localized plasticity facilitating accelerated nucleation of cracks [2]. More work in this area, with a bridge to the CM department is underway through the appointment of a postdoctoral scientist joint between the groups of T. Hickel and B. Gault's ERC-Consolidator Grant (see p. 70), and the development of further infrastructure for gas-charging in collaboration with M. Rohwerder's group.

References

1. Breen, A.J.; Mouton, I.; Lu, W.; Wang, S.; Szczepaniak, A.; Kontis, P.; Stephenson, L.T.; Chang, Y.; da Silva, A.K.; Liebscher, C.H.; Raabe, D.; Britton, T.B.; Herbig, M.; Gault, B.: Scripta Mater 156 (2018) 42.

2. Chang, Y.; Breen, A.J.; Tarzimoghadam, Z.; Kürnsteiner, P.; Gardner, H.; Ackerman, A.; Radecka, A.; Bagot, P.A.J.; Lu, W.; Li, T.; Jägle, E.A.; Herbig, M.; Stephenson, L.T.; Moody, M.P.; Rugg, D.; Dye, D.; Ponge, D.; Raabe, D.; Gault, B.: Acta Mater 150 (2018) 273.

Combining Advanced Electron Microscopy Techniques with Atom Probe Tomography and Density-Functional Theory to Understand Materials' Behaviours

C. Liebscher [2], T. Schwarz [1], M.J. Yao [1], P. Dey [3], I. Mouton [1], G. Stechmann [1], T. Hickel [3], D. Ponge [1], L.T. Stephenson [1], S. Zaefferer [1], G. Dehm [2], J. Neugebauer [3], C. Scheu [4], D. Raabe [1], M. Herbig [1], B. Gault [1]

[1] Department of Microstructure Physics and Alloy Design (MA)
[2] Department of Structure and Nano-/ Micromechanics of Materials (SN)
[3] Department of Computational Materials Design (CM)
[4] Independent Max Planck Group on Nanoanalytics and Interfaces (NG)

Over the past decades, it has become clear that understanding the interplay between structure, composition and properties requires the combination of advanced characterization techniques with compatible yet complementary strength. Electron microscopy and atom probe tomography form a good match as the former lacks the precise ppm-level compositional information whereas the latter does not allow for full structural analysis. In combination with *ab initio* simulation, which resolve their underlying chemo-mechanical coupling, a powerful toolbox for materials characterization becomes available.

A first example can be found in the combination of atom probe tomography with transmission Kikuchi diffraction. This technique exploits the diffraction of the electrons that have gone through the specimen to retrieve the local structure and grain orientation within the specimen. This is illustrated in Fig. 1, where a grain boundary is clearly imaged and characterized crystallographically in terms of its misorientation as well as chemically in terms of its local composition measured by atom probe. The study reveals strong segregation of Na and K impurities to the grain boundary in a $Cu(In,Ga)Se_2$ thin film used for solar cell application [1]. These solutes affect the degree of passivation of the grain and hence the transport properties of the film and the performance of the solar cell.

Moving up in scale, high-resolution scanning transmission electron microscopy (STEM) was performed on an atom probe specimen to reveal the atomic-scale structure of the material. A high-Mn weight-reduced Al-containing austenitic steel, strengthened by precipitation of coherent ordered κ-carbides upon heat treatment at 600°C was characterized [2]. Electron microscopy reveals the structure of the precipitates and their coherent interface with the matrix, as well as the local strain in the matrix with near-atomic resolution through advanced data processing. This information can be correlated with the compositional roughness of the interface observed in the atom probe data. The level of chemo-structural details from both techniques allowed to directly bridge to density functional theory calculations in order to understand how elastic strain fields impact the local concentrations of alloying elements at the atomic scale [3].

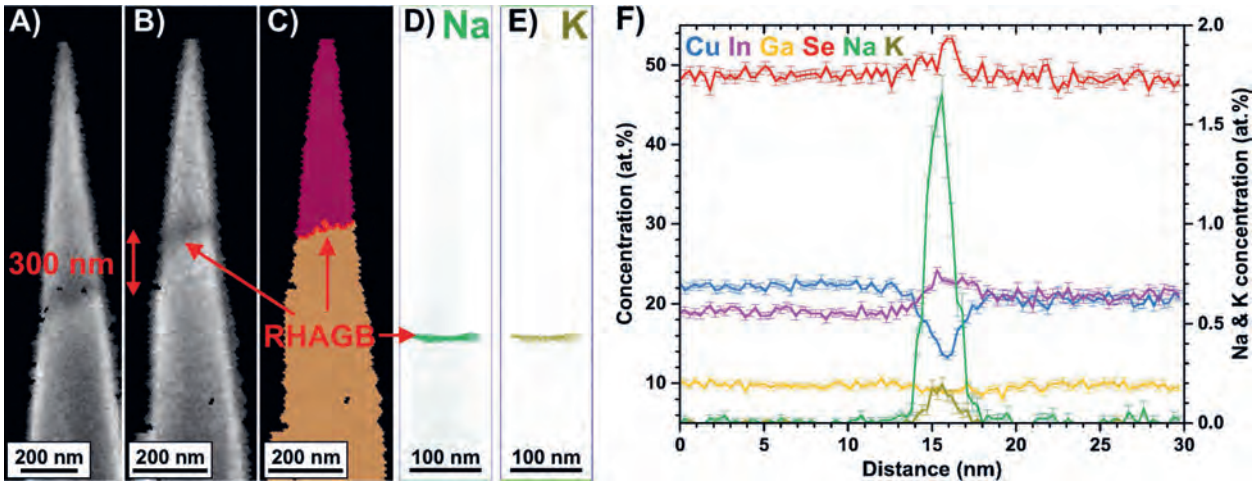

Fig. 1: *(A,B) Image quality maps from a transmission Kikuchi diffraction measurement taken directly on an atom probe tomography specimen. The dark contrast corresponds to a random high angle grain boundary (C) with a disorientation angle of 37.8°around the [201] axis. (D,E) Reconstructed atom probe data showing the Na and K distributions. (F) composition profile across the grain boundary reveals clear segregation [1].*

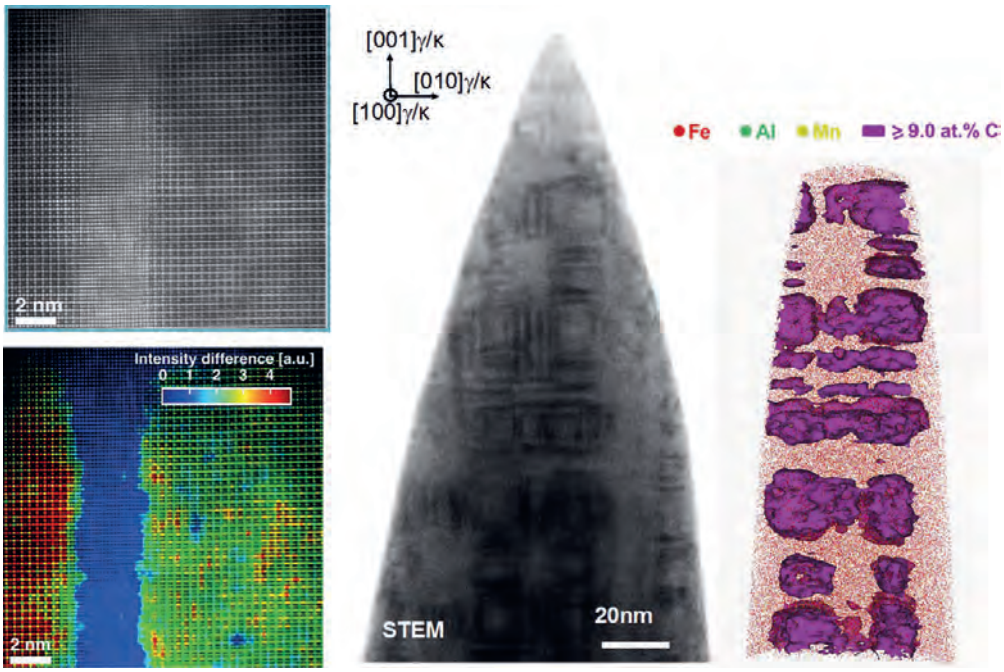

Fig. 2: *a) The close-up images are a high-angle-annular dark field (HAADF) image showing individual atomic columns that differ between the ordered precipitates (κ) and the matrix, as well as the corresponding atomic resolution strain ε_{xx} map. b) Annular bight field (ABF) STEM image of a needle-shaped specimen showing cuboidal κ-carbides in an austenitic matrix. The corresponding reconstructed atom probe data is shown to scale and highlights the C distribution. c) The ab initio calculations explain how strain and the solubility of C in the matrix are connected [3].*

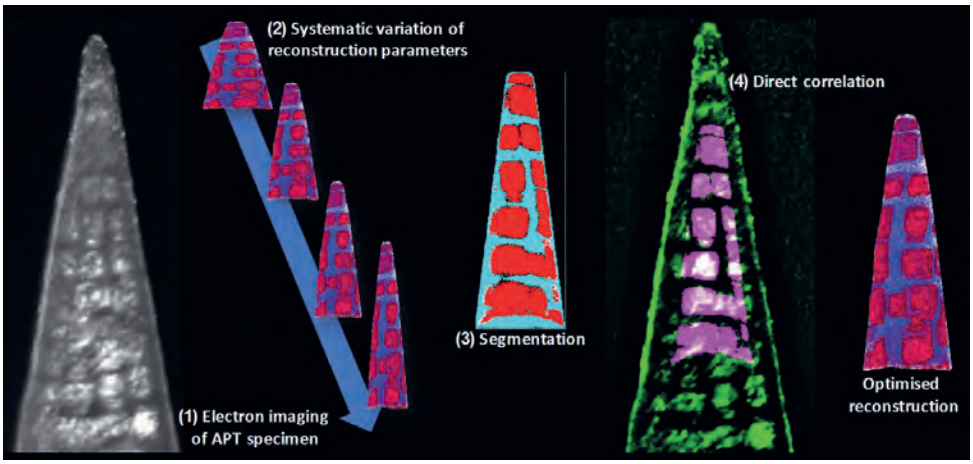

Fig. 3: *Step by step workflow for improving the fidelity of atom probe tomography reconstructions via digital image correlation with a transmission electron micrograph of the specimen acquired prior to the analysis [3].*

Finally, although significant effort was dedicated to developing protocols for correlative electron microscopy, atom probe tomography [4] as well as density functional theory (see p. 191), little has been done to truly combine the two streams of data and inform one technique with the results from the other. Here, we developed an approach that involved cross-correlation of a simulated electron image corresponding to the atom probe data with the electron micrograph of the specimen acquired prior to analysis. By systematically exploring the parameter space for reconstructing atom probe data and the possible rotations of the dataset with respect to the specimen, the results of the correlation is an optimised reconstruction of the atom probe data [5], as outlined in Fig.3.

References

1. Schwarz, T.; Stechmann, G.; Gault, B.; Cojocaru-Mirédin, O.; Würz, R.; Raabe, D.: Prog Photovoltaics 26 (2018) 196.
2. Yao, M.; Welsch, E.D.; Ponge, D.; Haghighat, S.M.H.; Sandlöbes, S.; Choi, P.-P.; Herbig, M.; Bleskov, I.; Hickel, T.; Lipinska-Chwalek, M.; Shanthraj, P.; Scheu, C.; Zaefferer, S.; Gault, B.; Raabe, D.: Acta Mater 140 (2017) 258.
3. Liebscher, C.; Yao, M.; Dey, P.; Lipińska-Chwalek, M.; Berkels, B.; Gault, B.; Hickel, T.; Herbig, M.; Mayer, J.; Neugebauer, J.; Raabe, D.; Dehm, G.; Scheu, C.: Phys Rev Mat 2 (2018) 023804.
4. Herbig, M.: Scripta Mater 148 (2018) 98.
5. Mouton, I.; Katnagallu, S.; Makineni, S.K.; Cojocaru-Mirédin, O.; Schwarz, T.; Stephenson, L.T.; Raabe, D.; Gault, B.: Microsc & Microanal (2019) accepted.

Towards High Stiffness and Damage Tolerance: Mo_2BC as a Model Material

S. Gleich [1], R. Soler [2], J.-O. Achenbach [3], C. Kirchlechner [2], G. Dehm [2], C. Scheu [1], J.M. Schneider [3,4]

[1] Independent Max Planck Research Group on Nanoanalytics and Interfaces (NG)
[2] Department of Structure and Nano-/ Micromechanics of Materials (SN)
[3] Max Planck Fellow Group on Self-Reporting Materials
[4] RWTH Aachen University

High stiffness commonly comes at the expenses of a poor damage tolerance, as high strength and high fracture toughness have been traditionally found to be self-excluding. However, some materials have the promise to combine these properties. Mo_2BC was predicted by *ab initio* calculations to exhibit both, an exceptional stiffness with a high Young's modulus of up to 470 GPa and a bulk modulus to shear modulus ratio indicating the possibility for moderate ductility [1]. Thus, from the calculated electronic structure point of view Mo_2BC has the potential to combine the traditionally conflicting properties of high stiffness and damage tolerance. To explore whether this unusual combination can be confirmed by experiments, magnetron sputtering at different substrate temperatures was used to synthesize Mo_2BC films for further studies by mechanical testing and microstructure characterization. First nanoindentation tests confirmed the predicted high Young's modulus and revealed plasticity by a visible material pile-up at the edge of the indent [1]. Additionally, Mo_2BC coatings on ductile substrates exposed to tensile stresses were found to be significantly less prone to cracking than bench-mark TiAlN coatings [2]. Since the first screening experiments were successfully indicating damage tolerance, high stiffness and hardness, we decided to analyze the structure - property relationships in more detail.

Nanostructure, hardness and Young's modulus: The evolution of the nanostructure of Mo_2BC coatings was studied as a function of the growth temperature and linked to the corresponding mechanical properties [3,4]. X-ray diffraction studies and advanced transmission electron microscopy investigations revealed a strong substrate temperature influence on the crystallinity of the bipolar pulsed direct current magnetron sputtered Mo_2BC films. The coatings deposited at substrate temperatures between 380 °C to 630 °C range from partially amorphous for the coatings deposited at 380 °C to fully crystalline for the ones deposited at 630 °C (Fig. 1) [3]. This change in microstructure is also reflected in the mechanical response. The hardness and Young's modulus increased with increasing deposition temperature from 21 GPa to 28 GPa and 259 GPa to 462 GPa, respectively. We attributed this increase to the change in the nano- and microstructure and the corresponding changes in the average bond strength and stiffness [3]. Advanced scanning transmission electron microscopy studies in conjunction with atom probe tomography revealed a large number of defects within all deposited films. For example, Ar-rich Mo-B-C disordered clusters with a diameter of about 1.5 nm were observed in the films which are related to the magnetron sputtering process [3]. Besides these disordered clusters, the fully crystalline films deposited at 630 °C possess structural features at various length scales [3,4]. There are bundles of co-

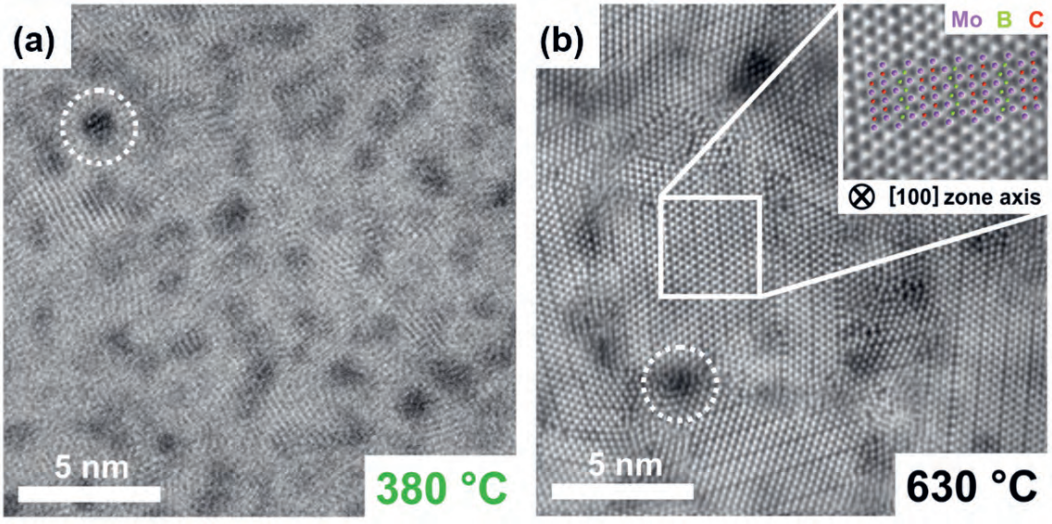

Fig. 1: *Plan-view scanning transmission electron microscopy images of the Mo_2BC films deposited (a) at 380 °C and (b) 630 °C. Exemplary, Ar-rich Mo-B-C disordered clusters are marked by dotted circles. The enlarged region of the grain interior in (b) shows the stacking sequence in [100] orientation. The figures are taken from [3].*

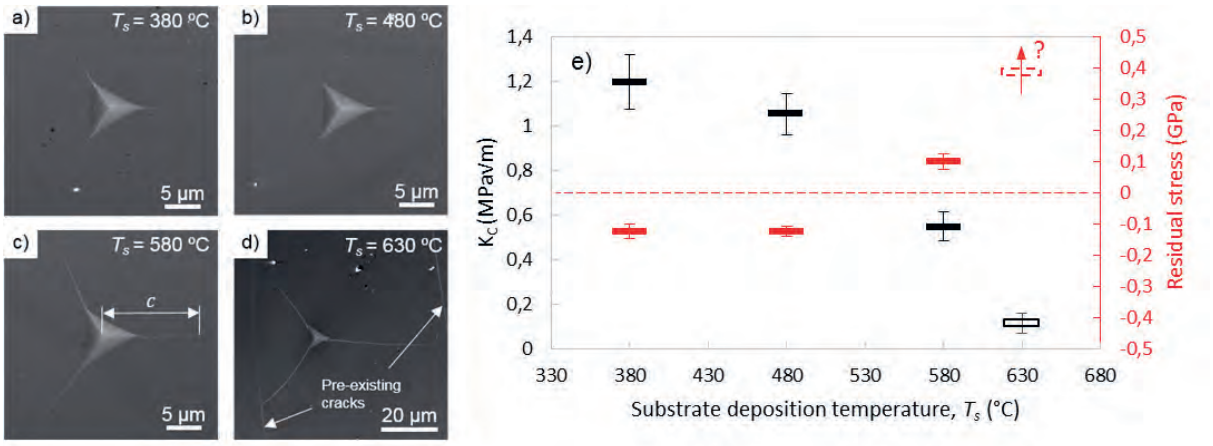

Fig. 2: *Nanoindentation induced cracks in Mo_2BC coatings deposited on Si substrates at a) 380 °C, b) 480 °C, c) 580 °C and d) 630 °C. The film stresses and apparent fracture toughness of the Mo_2BC films attached to the substrate are clearly related [6].*

lumnar grains (~10 nm in diameter) with dimensions of up to several micrometers in growth direction [4]. The atoms at the grain boundaries are less ordered compared to the grain interior, where stacking faults are present [4]. The thermal stability of the films was investigated by *ex situ* and *in situ* X-ray diffraction and transmission electron microscopy [5]. The partially amorphous film deposited at 380 °C transformed to fully crystalline during annealing resulting in grain sizes up to 1 µm at elevated temperatures. Up to 840 °C the interface to the Si substrate remained intact without delamination [5].

Fracture toughness studies of Mo_2BC: In order to obtain information on the fracture toughness, two different approaches were selected [6]. Indentation induced crack initiation was chosen to obtain the fracture toughness of the films attached to the substrate while notched cantilevers were used to obtain the fracture toughness of the films itself. The films grown at substrate temperatures of 380 and 480°C exhibit compressive stresses after cooling to room temperature, whereas the film grown at 580 °C shows tensile stresses after cooling [6]. The tensile stresses of the 630 °C deposited film are even larger, causing cracks when cooling down to room temperature, thus only a lower bound of the tensile film stress can be measured by wafer curvature with 0.4 GPa. Interestingly, indentation induced fracture leads to a lower apparent fracture toughness for the films grown at 630 °C compared to the lower deposition temperatures (Fig. 2). In contrast, notched cantilevers reveal the opposite trend, the higher the deposition temperature and crystallinity, the tougher the Mo_2BC coating with a maximum average fracture toughness of 4.7±0.52MPa√m for the fully crystalline film deposited at 630 °C. The linear elastic slope during loading of the notched beams does not indicate plasticity. This is also supported by fractography revealing brittle fracture. However, fractography indicates intergranular fracture along the columnar grain boundaries of the grains with their nanometer sized column diameters [6]. Future experiments on large grained Mo_2BC are required to resolve the fracture toughness of the bulk and to analyze dislocation plasticity.

References

1. Emmerlich; J.; Music, D.; Braun, M.; Fayek, P.; Munnik, F.; Schneider, J. M.: J. Phys. D: Appl Phys 42 (2009) 185406.
2. Djaziri, S.; Gleich, S.; Bolvardi,H.; Kirchlechner, C; Hans, M.; Scheu, C.; Schneider; J. M.; Dehm, G.: Surf Coat Technol 289 (2016) 213.
3. Gleich, S.; Soler, R.; Fager, H.: Bolvardi, H.; Achenbach, J.-O.; Hans, M.; Primetzhofer, D.; Schneider, J. M.; Dehm, G.; Scheu, C.: Materials & Design 142 (2018) 203.
4. Gleich, S., Fager, H.; Bolvardi, H.; Achenbach, J.-O.; Soler, R.; Pradeep, K. G.; Schneider, J. M.; Dehm, G.; Scheu, C.: J Appl Phys 122 (7) (2017) 075305.
5. Gleich, S., Breitbach, B.; Peter, N. J.; Soler, R.; Bolvardi, H.; Schneider, J. M.; Dehm, D.; Scheu, C.: Surf Coat Technol 349 (2018) 378.
6. Soler, R., Gleich, S.; Kirchlechner, C.; Scheu, C.; Schneider, J. M.; Dehm, G.: Materials & Design 154 (2018) 20.

Synthesis and High-Throughput Methods for High-Entropy Alloys

Z. Li [1], H. Springer [1], D. Raabe [1], F. Körmann [2], C. Kirchlechner [3], C. Liebscher [3], W. Lu [3], G. Dehm [3], A. Ludwig [4]

[1] Department of Microstructure Physics and Alloy Design (MA)
[2] Department of Computational Materials Design (CM)
[3] Department of Structure and Nano-/ Micromechanics of Materials (SN)
[4] Institute for Materials, Ruhr-Universität Bochum

High-entropy alloys (HEAs) are multi-component metallic materials consisting of four or more elements in high or even equimolar fractions [1-3]. The number of compositions explored is increasing rapidly due to the growing research efforts in this field driven by some promising mechanical HEA properties such as high fracture toughness at cryogenic temperatures. The main challenge that HEA research is facing is how to efficiently explore their huge compositional and microstructural spaces for novel materials with promising property profiles. Therefore, we have been working on different approaches for the combinatorial and high-throughput synthesis and processing of HEAs [3].

The first approach we employed is rapid alloy prototyping (RAP) which is a semi-continuous high-throughput bulk casting, rolling, heat treatment and sample preparation method developed at the MPIE, and has been successfully applied to screening weight-reduced TWIP-type steels, high strength martensitic steels and HEAs [3,4]. The RAP approach enables casting of five different alloys with tuned compositions of an alloy system in one operation. This is achieved by using a set of five copper moulds which can be moved stepwise inside the furnace. Following casting, the alloy blocks with a thickness of 10 mm and varying compositions are subsequently hot-rolled in air. This step is required for removing dendrites and casting porosity. After the final hot-rolling pass, the HEA plates are homogenized at high temperatures (e.g., 1200 °C) for several hours (e.g., 2 h) under Ar atmosphere, followed by water quenching. Since the homogenized HEA plates generally exhibit a large grain size, cold-rolling and annealing are required for refining the microstructure towards better mechanical properties. Thickness reduction by cold-rolling is generally higher than 50% to obtain a sufficiently high driving force for primary recrystallization. After these microstructure-tuning processing steps, samples for microstructure investigation and performance testing are machined from the alloy segments by spark erosion. Various characterization methods are then used for probing composition-microstructure-property relationships (Fig. 1).

The second high-throughput method for multi-component HEAs is utilizing diffusion multiples which can serve for alloy synthesis through systematic intermixing among blocks of pre-alloyed composition [3]. This allows three or more metal blocks to be placed in diffusional contact. Generally, such diffusion-multiple setups are subjected to a high temperature to induce thermal inter-diffusion to form continuously compositionally graded solid solutions and/or intermetallic compounds. In a diffusion-multiple assembly, the contacted surfaces of different metal blocks are required to be polished and cleaned without contamination. The aggregates are then treated in a hot isostatic pressing (HIP) process at high temperature (e.g., 1200 °C) for several hours to achieve intimate interfacial contacts of all constituent blocks. Subsequently, the diffusion multiple is heat-treated at a high tem-

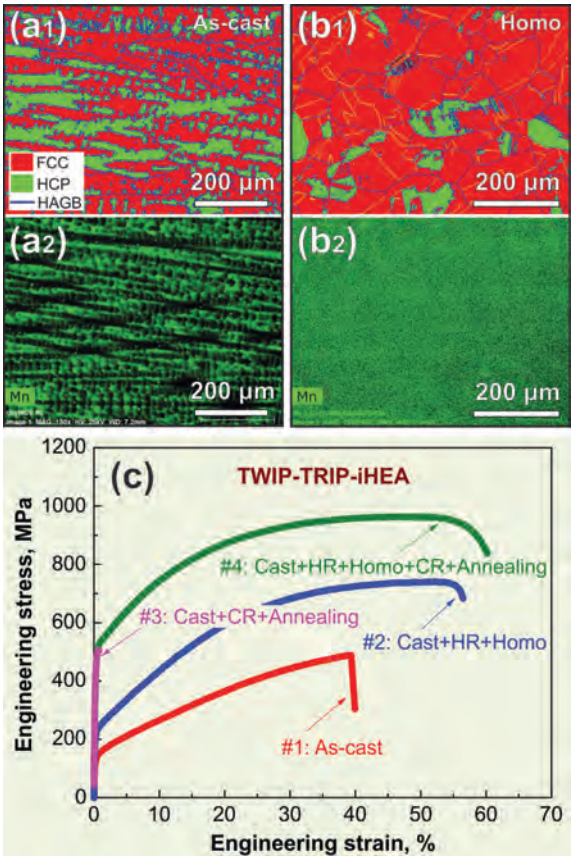

Fig. 1: *Microstructure, compositional homogeneity state (a,b) and tensile properties (c) of an interstitial high-entropy alloy ($Fe_{49.5}Mn_{30}Co_{10}Cr_{10}C_{0.5}$, at. %) in different processing conditions obtained after specific steps of rapid alloy prototyping [3]. FCC, HCP and HAGB refer to face-centred cubic phase, hexagonal close-packed phase and high-angle grain boundaries, respectively. "HR", "Homo" and "CR" refer to hot-rolling, homogenization and cold-rolling, respectively.*

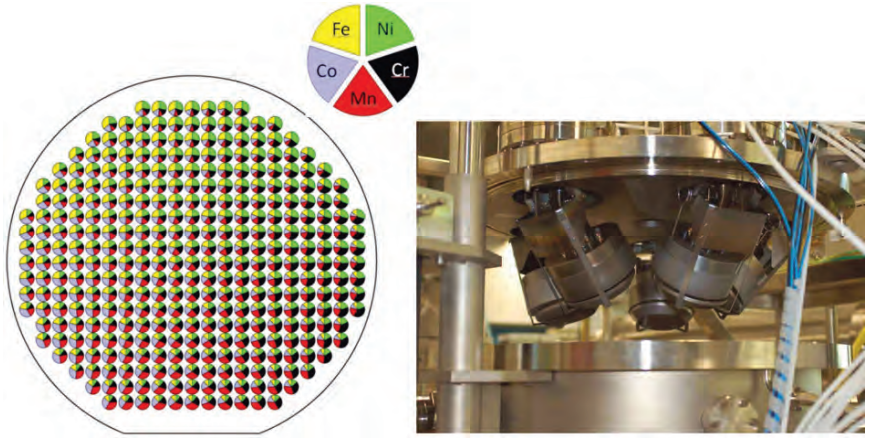

Fig. 2: *Field with varying quinary HEA compositions contained in a thin-film library of Cr-Mn-Fe-Co-Ni co-sputtered from individual single-element targets, indicating the relative concentrations at each of 342 EDS measurement points (EDS: energy dispersive X-ray spectroscopy). The legend identifies the elements and respective cathode positions in an opened co-sputter chamber [3].*

perature (e.g., 1200 °C) for a long period (generally above 24 h). The total time of heat-treatment at high-temperature is determined for achieving diffusion profiles with sufficiently large extension, so that the solid-solution phases and/or intermetallic compounds formed in the diffusion-multiple are large enough to be subsequently characterized without interference from neighbouring phases [3].

The third approach for the high-throughput synthesis of HEAs is combinatorial laser additive manufacturing (LAM) enabling synthesis of compositionally graded materials which allows many variants to be probed efficiently for instance by using established micromechanical testing methods [3]. The compositionally gradient part can be designed to include large compositional steps, and it can also proceed with a smoothly graded transition from one composition to another. Also, metal-matrix-composites, e.g., nano-particle reinforced HEA-based materials, with a compositionally graded matrix can be fabricated by LAM. This can be realized when one of the powders being transferred into the laser has a significantly higher melting temperature than the others, thereby avoiding that particles pre-alloy with powders of lower melting point [3].

The fourth high-throughput technique used for probing the large HEA space is pursued together with A. Ludwig at the Ruhr-Universität Bochum. His group synthesizes multinary thin-film materials libraries, i.e. well-defined and large thin-film composition gradients across a substrate wafer fabricated in a single experiment. Co-deposition from cathodes that are tilted with respect to the substrate plane results in wedge-shaped nanoscale thin films that are thickest from the geometrically closest edge of the substrate to thinnest at the farthest edge. Multiple cathodes evenly distributed around the centre of a substrate (3 cathodes: 120° separation, 4 cathodes: 90° separation, 5 cathodes: 72° separation) each produce such a wedge, with the resulting composition at any point on the substrate being the sum of the material arriving from each cathode (Fig. 2). Co-sputtered films are atom-scale mixtures of the materials that are often subsequently annealed to form thermodynamically stable phases and reduce defects.

To promote the efficient high-throughput development of HEAs, theoretical guidance is critically important, capable of suggesting suited mechanical or magnetic trends for the design of alloy compositions [5]. For instance, to design strong, tough and ductile HEAs, we found that phase (meta)stability of HEAs is an important feature which can be well tuned in terms of composition adjustment to introduce activation of athermal deformation mechanisms (TWIP/TRIP), thereby improving the range of accessible strength-ductility combinations [2,5]. Accordingly, parameter-free *ab initio* simulations and thermodynamic calculations are used to provide guidance for adjusting stacking fault energies and/or free energy differences between phases to assist the high-throughput HEA development [5].

References

1. Yeh, J.W.; Chen, S.K.; Lin, S.J.; Gan, J.Y.; Chin, T.S.; Shun, T.T.; Tsau, C.H.; Chang, S.Y.: Adv Eng Mater 6 (2004) 299.
2. Li, Z., Pradeep, K.G., Deng, Y., Raabe, D., Tasan, C.C.: Nature 534 (2016) 227.
3. Li, Z., Ludwig, A., Savan, A., Springer, H., Raabe, D.: J Mater Res (2018) in press.
4. Springer, H., Raabe, D.: Acta Mater 60 (2012) 4950.
5. Li, Z., Körmann, F., Grabowski, B., Neugebauer, J., Raabe, D.: Acta Mater 136 (2017) 262.

A Rare-Earth Free Magnesium Alloy with Improved Intrinsic Ductility

S. Sandlöbes [1,4], M. Friák [2,3], S. Korte-Kerzel [1], Z. Pei [3,5], J. Neugebauer [3], D. Raabe [4]

[1] now at: Institute of Physical Metallurgy and Metal Physics, RWTH Aachen University, Germany
[2] now at: Institute of Physics of Materials, Academy of Sciences of the Czech Republic, Czech Republic
[3] Department of Computational Materials Design (CM)
[4] Department of Microstructure Physics and Alloy Design (MA)
[5] now at: Oak Ridge National Laboratory, Tennessee, USA

Magnesium and its alloys have a hexagonal crystal structure. Their wider application is hindered by their poor ductility. The lack of room temperature formability is caused by deformation being confined to $\{0001\}\langle 11\bar{2}0\rangle$ basal <a> dislocation slip which does not allow accommodation of strain along the crystal c-axis (Fig. 1).

Strain along the crystal c-axis can only be accommodated by the activation of non-basal slip in hexagonal crystals, i.e. it is crucial for compatible polycrystalline deformation of Mg [1]. Alloying with yttrium and rare earth (RE) elements has been shown to improve the room temperature ductility [1-3]. Recent studies revealed that such ductility increase in Mg-Y and Mg-RE alloys is caused by <c+a> dislocation slip providing out-of-basal-plane shear [1-3].

The activation of out-of-basal-plane shear through Y or RE elements in Mg is correlated with a decreased I_1 intrinsic stacking fault energy (I_1 SFE). The I_1 SFE decreases with increasing Y and RE concentration. This is used here as a parameter connected with the ductility increase in the Mg-Y and Mg-RE systems. We conducted *ab initio* assessments of the thermodynamic, energetic (elastic energy) and structural-volumetric interactions of yttrium and RE atoms in Mg in solid solution and their effects on the I_1 SFE to understand the origin of slip system selection. We developed a quantum mechanically guided treasure map for Mg alloying [4,5]. The idea is to start from a Mg-Y alloy that is ductile, yet, is commercially not attractive, and search for alloy compositions matching the reference system as closely as possible for selected element-specific properties. This proximity between two alloys is expressed by a similarity index $Y_c=1-\{\sum_\alpha w_\alpha(\alpha - \alpha_c)^2\}^{1/2}$ where the subscript c describes the chemical composition of the new alloy, α describes a selected set of element-specific properties and w_α are the weighting factors. This proximity factor Y_c is referred to as yttrium-similarity index, YSI.

To determine a set of elemental properties and weighting factors we used density-functional theory to compute reference quantities for a set of solid-solution binary $Mg_{1-x}X_x$ alloys (x<<1) [4,5]. We identified three correlations: the atomic volume of pure solutes, their electronegativity and their bulk modulus. From the correlation coefficients we obtained the weight, w_α. We screened 2850 ternary combinations (Fig. 2a) and identified 17 ternary alloys highlighted in Fig. 2b with YSI values ≥ 0.95. Fig. 2a shows a symmetric matrix of all 2850 solute pairs computed, where the respective solutes are given on the x- and y-axes. The intersection points of each solute pair of the y- and x-axis are marked by a coloured

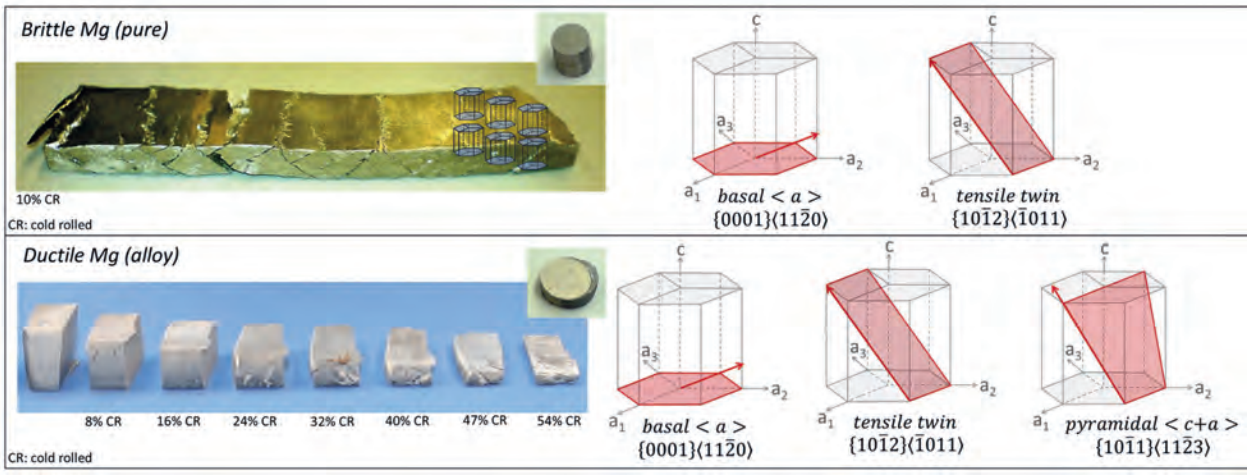

Fig. 1: *Pure polycrystalline magnesium fails brittle already at low strains (top row). The new Mg-1Al-0.1Ca alloy can be cold rolled to 54% thickness reduction (bottom row) [5].*

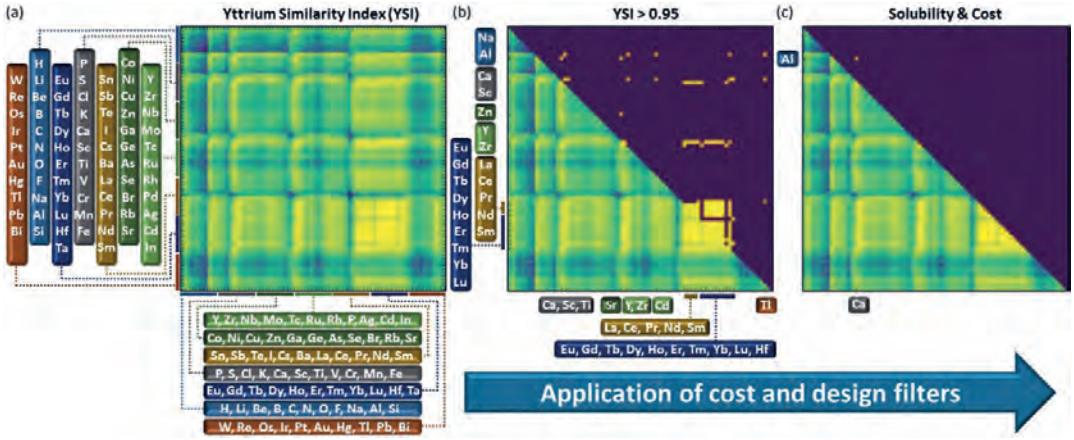

Fig. 2: *Yttrium-similarity index, YSI for the 2850 solute pairs computed in this study and visualized in the form of a symmetric matrix (a) with yellow indicating a high similarity and blue a low one. Solute pairs that have a high index (YSI>0.95) are shown in the upper triangular part in (b). Applying a cost and solubility filter only a single pair, Al-Ca, remains (c) [5].*

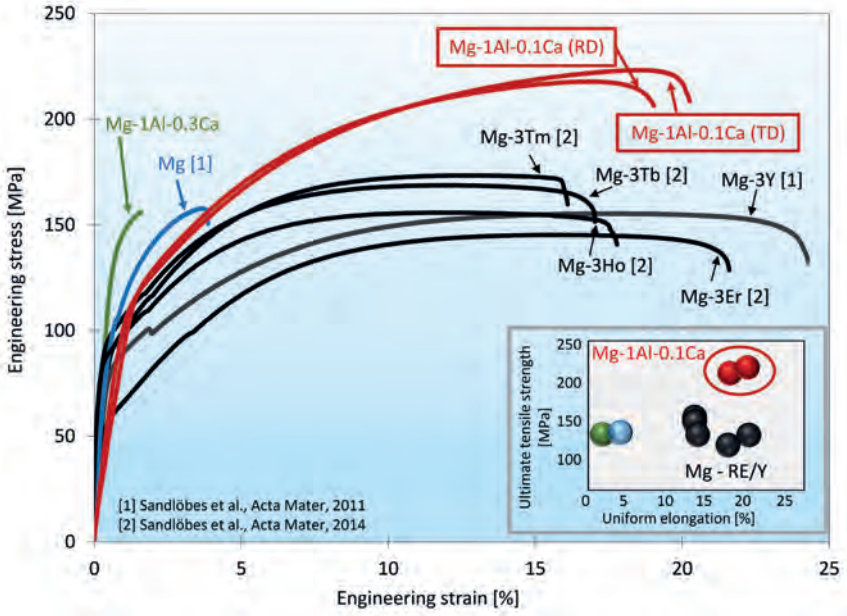

Fig. 3: *Engineering stress-strain curves of the new Mg-Al-Ca alloy shown in Fig. 1 in comparison with solid solution Mg-Y, Mg-RE, pure Mg and Mg-Al-0.3Ca [5]. The inset shows the ultimate tensile strength – uniform elongation diagram of the same alloys. RD: rolling direction; TD: transverse direction. Compositions in weight %.*

point indicating the similarity of that pair to Y. Yellow colour corresponds to a high similarity to Y (high YSI) and blue to a low YSI. In the upper triangle of Fig. 2b only those solute pairs with an YSI above 0.95 (i.e. 95% or higher similarity to Y) are shown. The solutes are listed at the x- and y-axis in Fig. 2b. From this list 11 alloys are RE/Y-free. We applied a second filter ruling out element pairs which are incompatible with recycling constraints, toxic, not sufficiently soluble in Mg or too expensive so that only one alloy system remains, viz. Mg-Al-Ca [4-6]. With this result we synthesized a new material, namely, Mg-1Al-0.1Ca (wt.%). Fig. 3 shows the tensile stress-strain behaviour of the new alloy in comparison with pure Mg and binary solid solution Mg-RE and Mg-Y alloys revealing superior mechanical properties.

References

1. Sandlöbes, S., Zaefferer, S., Schestakow, I., Yi, S., Gonzalez-Martinez, R.: Acta Mater 59 (2011) 429.
2. Agnew, S.R., Yoo, M.H., Tome, C.N.: Acta Mater 49 (2001) 4277.
3. Sandlöbes, S., Friák, M., Zaefferer, S., Dick, A., Yi, S., Letzig, D., Pei, Z., Zhu, L.-F., Neugebauer, J., Raabe, D.: Acta Mater 60 (2012) 3011.
4. Pei, Z., Friák, M., Sandlöbes, S., Nazarov, R., Svendsen, B., Raabe, D., Neugebauer, J.: New J Phys 17 (2015) 093009.
5. Sandlöbes, S., Friák, M., Korte-Kerzel, S., Pei, Z., Neugebauer, J., Raabe, D.: Sci Rep-UK 7 (2017) 10458.
6. Zeng, Z.R., Bian, M.Z., Xu, S.W., Davies, C.H.J., Birbilis, N., Nie, J.F.: Mater Sci Eng A 674 (2016) 459.

Advanced Lightweight Steels

D. Ponge [2], T. Hickel [1], M. Herbig [2], B. Gault [2], S. Zaefferer [2], P. Shanthraj [2], F. Roters [2], C. Scheu [3], J. Neugebauer [1], D. Raabe [2]

[1] Department of Computational Materials Design (CM)
[2] Department of Microstructure Physics and Alloy Design (MA)
[3] Independent Max Planck Research Group on Nanoanalytics and Interfaces (NG)

High-Mn lightweight steels offer a very good combination of high strength, ductility and toughness together with a reduced mass density due to their high Al content. For clarifying the mechanisms responsible for the outstanding mechanical properties, we collaborated on this topic among several departments at the MPIE. The aim was to understand especially the origin of the high strain hardening rate in the as quenched state (devoid of κ-carbides) [1] and in the precipitation hardened state (containing L'1_2-type κ-carbides) and the mechanisms of precipitation hardening [2]. For this purpose, the microstructure evolution of a high-Mn lightweight steel (Fe-30.4Mn-8Al-1.2C, wt.%) was studied after interrupted tensile testing by electron channeling contrast imaging (ECCI), transmission electron microscopy (TEM), atom probe tomography (APT) and correlative TEM/APT. To quantify the precipitation strengthening, the anti-phase boundary (APB) energy of the $(Fe,Mn)_3AlC$ κ-carbides was determined by *ab initio* calculations. The seemingly inconsistent outcomes of theory and experiment led to new insights into the mechanisms of precipitation strengthening in these steels.

Strain hardening: Interestingly, the material deforms in both conditions (as quenched or precipitation hardened) by planar slip, indicating a low cross slip frequency. This results in a low rate of dynamic recovery and, therefore, a high apparent strain hardening rate. Here, we observe a gradual reduction of the spacing between the co-planar slip bands with increasing strain, which leads to constantly high strain hardening (Fig. 1). To further confirm this mechanism, the flow stress was calculated from the coplanar slip band spacing on the basis of the dislocation passing stresses. The good agreement between the calculated values and the tensile test data confirms that dynamic slip band refinement is the main strain hardening mechanism.

Precipitation hardening is increasing the yield stress, but the strain hardening behaviour is nearly the same like in the κ free condition (Fig. 1). Again planar slip and dynamic slip band refinement were identified as governing deformation mechanisms. The resulting strain hardening rate is high enough to compensate the negative strain hardening rate caused by shearing and fragmenting the *κ*-carbide precipitates. The latter is connected with dislocation penetration and the dragging out of carbon and other elements by these dislocations, which leads

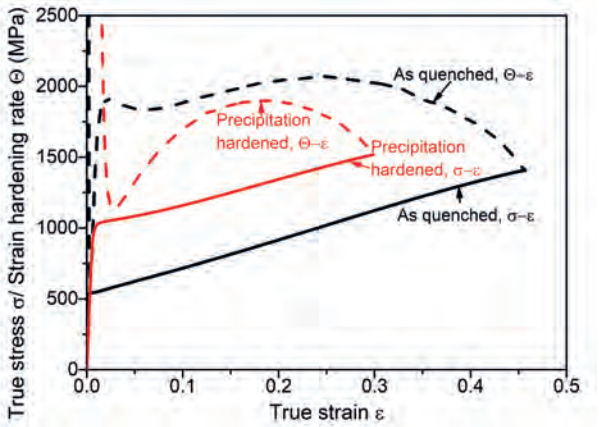

Fig. 1: *True stress-strain curve of the alloy in precipitation hardened state (red solid line) in comparison to that of the alloy in the as quenched state (black solid line). The strain hardening curves Θ–ε of both states are shown as dashed lines.*

to a reduction of the APB energy in the κ-carbides as detailed below. Especially at higher strains, the shearing and fragmentation of the *κ*-carbides leads to a reduction of the apparent strain hardening rate in comparison to the as quenched state.

Precipitation hardening: A heat treatment at 600°C for 24 h resulted in the formation of *κ*-carbide precipitates and an increase in the proof stress. In order to better interpret the resulting hardening, the particle size, shape and inter-spacing needs to be analysed. This is ambiguous with TEM alone, since it only provides a 2D projected image of the microstructure. Therefore, to achieve a better topological characterization of the precipitate morphology and arrangement, APT analysis was performed. Fig. 2 shows a representative κ/γ microstructure observed in the reconstructed 3D atom maps by APT.

Fig. 3 shows TEM micrographs of a deformed sample. The whole precipitation structure is shown to be sheared along a fine line, indicating the shearing of κ-carbide precipitates by dislocations on the same glide plane.

To quantify the precipitation strengthening effect, the APB energy of the L'1_2 –type $(Fe,Mn)_3AlC$ κ-carbides has been determined by *ab initio* calculations. The energies for the stoichiometric carbides turned out to be much too high to explain the observed shearing by dislocations. We realized that this is related to a reduced C content in the precipitates. Instead of a stoichiometric C content of 20 at.%, the actual C concentration of κ-carbide is in the order

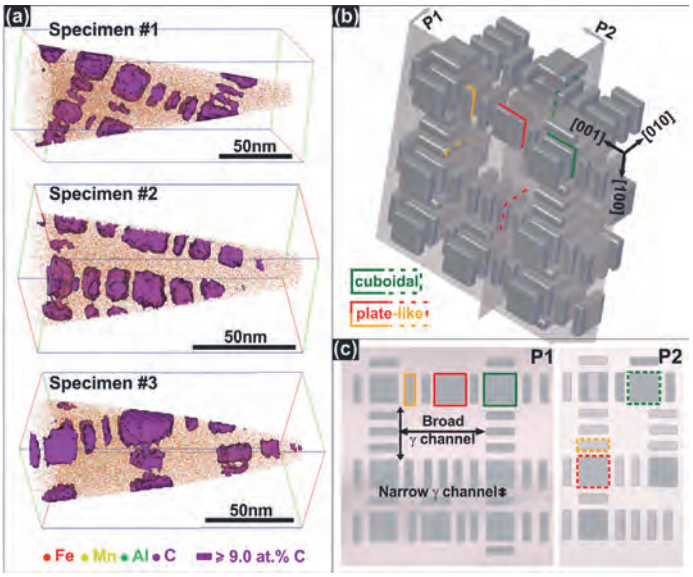

Fig. 2: *Morphology and arrangement of κ-carbide precipitates by APT (3D) and 2D sketches: (a) three representative reconstructed 3D APT maps of Fe (red), Mn (yellow), Al (green) and C (purple) atoms. The κ-carbide precipitates are visualized with 9 at.% C iso-concentration surfaces. (b) Schematic illustration of 3D morphology and arrangement of κ-carbide precipitates based on APT observations. (c) 2D projections of the κ/γ microstructure along <001> directions highlighted in (b), reflecting the TEM observations [2].*

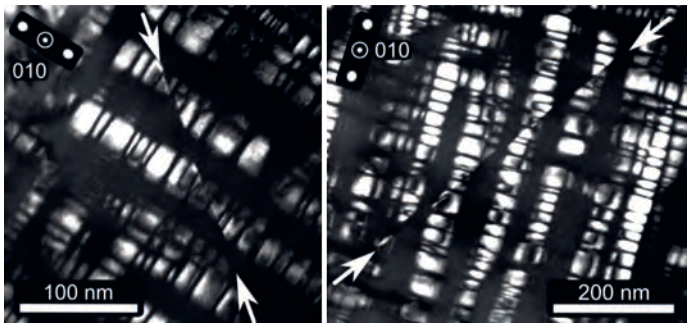

Fig. 3: *DF-TEM images showing sheared κ-carbides at a strain of 0.02 (with g=(010) superlattice reflection used for DF imaging and viewing direction close to the [110] zone axis) [2].*

of 13 at.% [3]. Therefore, two extreme cases were studied, namely, a full occupancy of the body-centred interstitial sites by C and a C-free $L1_2$ Fe_3Al structure. The resulting γ_{APB} value of κ-carbide in the current alloy is expected to lie in the range of ~350-700 mJ/m^2. The measured particle radius of around 10 nm indicates that for the given volume fraction of around 0.2, the strengthening is then in the range of 900-1800 MPa. However, experimentally, the κ-carbides introduced upon ageing were found to increase the yield strength only by ~500 MPa.

This discrepancy can be explained by the influence of dislocation pile-up stresses at the κ-carbide interfaces that assist particle shearing. The pile-up of dislocations in the grain interior has been observed in the as quenched state with short range ordering [1]. This is difficult to be captured by ECCI or TEM here in the precipitation hardened state due to the high number density of precipitates. Calculations [2] indicate that a pile-up size of 4-8 dislocations is required to reduce the macroscopic strengthening effect to ~500 MPa, which, based on previous experimental observations [1], is a reasonable assumption. An additional reason for the lower experimental yield strength increase by κ-carbide precipitation compared to the calculated value is the reduced concentration of alloying elements in the matrix due to κ-carbide formation. This leads to a reduced solid solution strengthening of the matrix and a reduced tendency for short range ordering [1]. Both mechanisms reduce the effective strengthening contributed by precipitation hardening.

References

1. Welsch, E.; Ponge, D.; Haghighat, S.M.H.; Sandlöbes, S.; Choi, P.; Herbig, M.; Zaefferer, S.; D. Raabe: Acta Mat 116 (2016) 188.
2. Yao, M.J.; Welsch, E.; Ponge, D.; Haghighat, S.M.H.; Sandlöbes, S.; Choi, P.; Herbig, M.; Bleskov, I.; Hickel, T.; Lipinska-Chwalek, M.; Shanthraj, P.; Scheu, C.; Zaefferer, S.; Gault, B.; Raabe, D.: Acta Mat 140 (2017) 258.
3. Dey, P.; Nazarov, R.; Dutta, B; Yao, M.J.; Herbig, M.; Friák, M.; Hickel, T.; Raabe, D.; Neugebauer, J.: Phys Rev B 95 (2017) 104108.

Deploying Machine Learning to Extract Meaningful Materials Science Information from Advanced Microscopy

S. Zhang [1], Y. Wei [2], A.J. Breen [2], M. Herbig [2], B. Gault [2], C. Scheu [1], C. Freysoldt [3], C. Liebscher [4]

[1] Independent Max Planck Group on Nanoanalytics and Interfaces (NG)
[2] Department of Microstructure Physics and Alloy Design (MA)
[3] Department of Computational Materials Design (CM)
[4] Department of Structure and Nano-/ Micromechanics of Materials (SN)

Advanced microscopy and spectroscopy offer unique opportunities to study the structure, composition, and bonding state of individual atoms from within complex, engineering materials. Such information can be collected at a spatial resolution of as small as 0.1 nm with the help of aberration correction. With advancements in electron source brightness and detection efficiency, acquiring spatial maps in 2D and even 3D has become a routine practice, generating ever bigger datasets to handle.

Researchers at the MPIE now routinely make use of tools from the big data community [1,2]. As an example, nonnegative matrix factorization (NMF) algorithms are applied to electron energy loss spectroscopy (EELS) datasets. Fig.1 shows a sparse representation of an EELS spectrum imaging, using three spectral components and their spatial contribution maps to approximate spectra from 500 pixels. The differences in spectral features and their spatial origins are presented without the need to inspect 500 individual spectra. For example, the Ti-L_3 edge of component 3 has a peak position shifted to the left compared to the other components, corresponding to a reduced oxidation state of Ti. The spatial maps of component 3 reveals such reduced species come from the interface between the TiO_2 nanoparticle and the AlOOH matrix [3].

Dimension reduction of big data benefits researchers not only in presenting the data. Also, the subsequent data handling becomes less exhaustive and the quantification less biased [2].

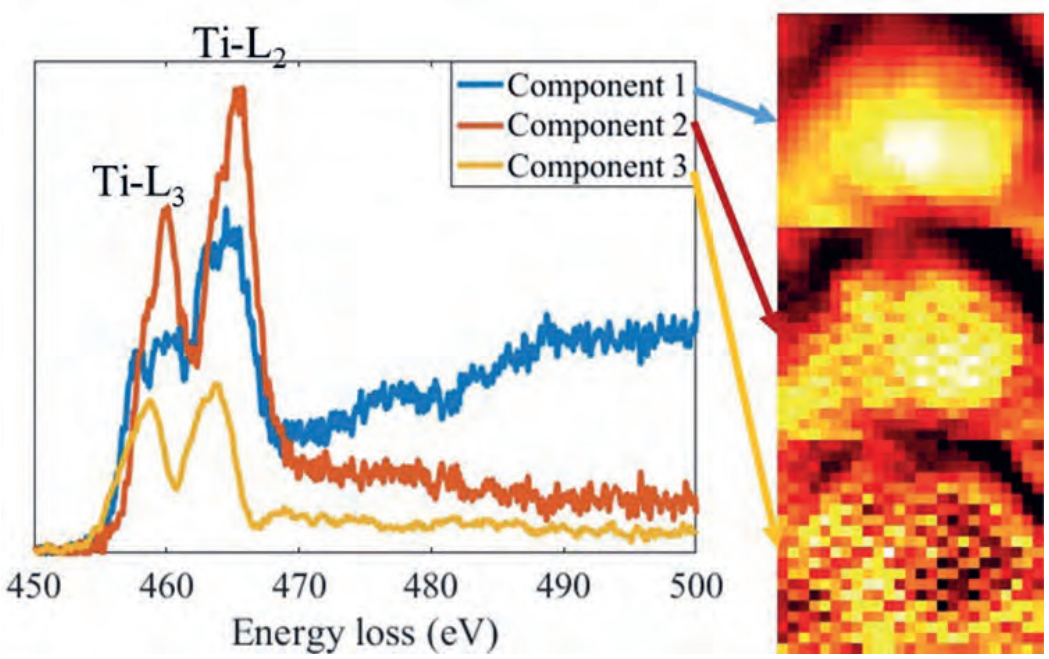

Fig. 1: *Three major spectral components of 500 electron energy loss spectra of Ti-L_3 and -L_2 edges, and their spatial contribution maps. The pixel size is 2 × 2 nm² [3].*

A second example came from the analysis of the field desorption patterns obtained from atom probe tomography (APT). APT maps the 3D position and chemical identity of up to a billion atoms in a material. The pattern formed on the single-particle detector often reveals traces of the crystallographic structure and orientation of the specimen. However, it remains largely under-utilised due to the lack of efficient and accurate extraction techniques. We have proposed a mixture of feature detection, machine learning and deep learning to enable automatic identification of crystallographic patterns observed on atom probe detector maps. Preliminary results exploiting theoretical geometric relationships have been very promising. A

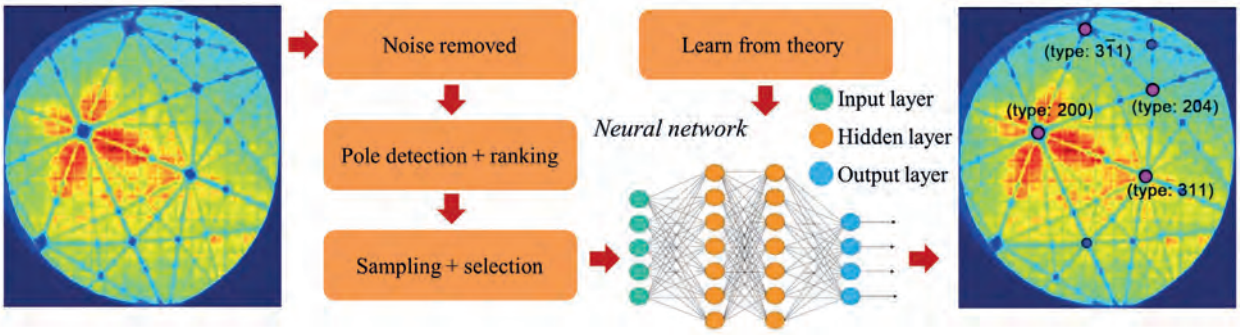

Fig. 2: *Complete workflow of automated identification of grain orientation via a deep neural network.*

flow-chart outlining this process is shown in Fig. 2. For detector hit-maps obtained from pure-Al specimens, our approach correctly characterised the orientation of single crystals with 98% confidence.

A database of experimental images for training was built, but for more complex materials systems and low-symmetry crystallographic structures there is not enough labelled data yet. This offers unique opportunities to bridge with the CM department. By full-scale, theory-driven forward calculations of such maps we can build large databases from which the machine learning algorithms will learn and refine the data analysis, as well as systematically explore the ultimate limits of APT crystallography in multi-phase multi-component samples.

Further forays into deploying big-data methodologies to advanced microscopies will be a future focus at the MPIE, as a collaborative project was recently awarded funding within the BigMax network (see p. 53) to pursue approaches to better evaluate large spectral dataset from scanning transmission electron microscopy (STEM) and extract atomic-scale compositional and structural information. In particular, we develop an automatic classification of high-resolution STEM image-series into distinct spatial regions according to the actual microstructure of the sample in order to detect, e.g., intra-grain variations or inter-grain differences even in very noisy data. Any advances in the analysis will be directly used to push the experimental measurement conditions to their limits.

References

1. Wei, Y; Gault, B.; Varanasi, R.S.; Raabe, D.; Herbig, M.; Breen, A.J.: Ultramicroscopy 194 (2018) 15.
2. Zhang, S.; Scheu, C.: Microscopy 67 (2018) 133.
3. Da Silva, N. L.; Jayasundera, A.C.; Folger, A.; Kasian, O.; Zhang, S.; Yan, C.-F.; Scheu, C.; Bandara, J.: Catal Sci Technol 8 (2018) 4657.

Ab initio-Derived Semiconductor Surface and Interface Phase Diagrams

L. Lymperakis [1], C. Freysoldt [1], S. Wippermann [2], J. Neugebauer [1]

[1] *Department of Computational Materials Design (CM)*
[2] *Department of Interface Chemistry and Surface Engineering (GO)*

III-V semiconductors have shaped optoelectronic technology for decades, and progressively enter power electronics, solar cells, and quantum technology. The bulk materials and nanostructures for actual devices are produced by controlled growth, be it in gas phase epitaxy, wet chemistry, or colloidal synthesis. Surfaces and interfaces therefore play a dominant role in determining the materials' properties. Surface effects may alter the chemical composition and provide routes to surface engineer growth in order to obtain materials with targeted properties. An alternative path to achieve tailored materials is the controlled wet-chemical assembly of dissimilar components into nanostructured materials. Both approaches depend critically on the ability to understand and control the physics and chemistry at the surfaces and at the interfaces. Here, we investigate these and highlight recent insights obtained by *ab initio* modelling into growth processes of semiconductor alloys and nanostructures.

Today's power light emitting diodes (LEDs) employ $In_xGa_{1-x}N$ alloys as active zone for light generation. While the $In_xGa_{1-x}N$ system allows for continuously tuning the colour from UV (pure GaN) to infrared (pure InN) in principle, the lack of homogeneous alloys with more than 30% Indium content forces us to down-convert blue light from low-In concentration devices. Detailed investigations on the bulk thermodynamics of these alloys suggest a favourable ordered phase at the technologically relevant In content of 33%, but only at low temperatures [1]. However, recent experimental findings indicate that this order even occurs at temperatures as high as 950 K. In order to resolve this discrepancy we employed DFT calculations and investigated In incorporation in the GaN(0001) surfaces. For growth under N rich conditions the (0001) III-Nitride surfaces reconstruct in order to obey the electron counting rule. The latter results in a 2×2 N adatom reconstruction which leaves ¾ of the surface metal atoms four-fold coordinated in a sp^3 configuration and ¼ of them triply coordinated in a planar sp^2 configuration. Although, the stronger Ga-N bonds are expected to result in preferential incorporation of In at the low coordinated surface sites, our calculations reveal a novel reconstruction mechanism, elastically frustrated rehybridization (EFR), that contradicts this conventional picture: due to their large atomic radius, In atoms at the triply coordinated sites are hindered from re-hybridizing to the sp^2 configuration [2]. Instead, they preferentially incorporate to four-fold coordinated surface sites where rehybridization of the triply coordinated Ga is allowed.

The effect of the above mentioned EFR mechanism on the alloy compositional limits is significant. We have calculated the chemical potential of In at the surface as a function of the surface In content. As it is revealed in Fig. 1 the chemical potential remains essentially flat for low surface In contents where In is substituted only at sites obeying the EFR mechanism. However, increasing the In concentration from ¼ to

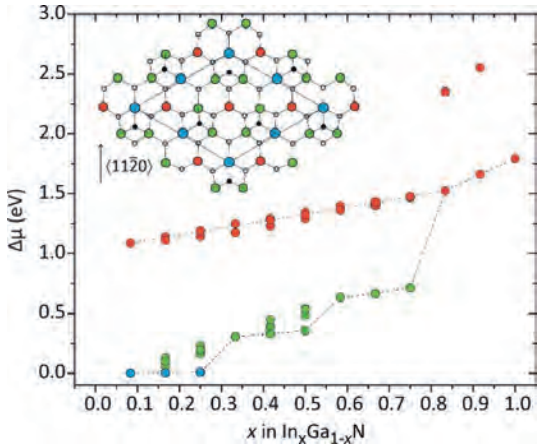

Fig. 1: *Chemical potential Δμ of In at the surface as a function of composition x. Green/blue and red dots correspond to the lowest- and higher-energy configuration/s for each x, respectively. The dashed lines are guidelines for the eye. (Inset) Top view of the lowest energy (2√3 x 2√3)R30° $In_{0.25}Ga_{0.75}N$ reconstruction. Small/black dots denote the N adatoms and small/open balls the N atoms. Blue balls indicate the In atoms and red and green balls the ×3 and ×4 coordinated inequivalent Ga atoms, respectively.*

⅓ increases the In chemical potential by ~ 0.3 eV, cf. Fig. 1. This corresponds to a ≈5-fold increase of the In-flux in molecular beam epitaxy growth (MBE). Such a huge increase in the In-flux would eventually switch the growth conditions to In-rich, resulting in the formation of In droplets and poor growth morphology. These trends in the computed chemical potential as function of the In content explain the observed experimental limitations in achieving higher In concentrations. Nevertheless, EFR may also provide efficient pathways to surface engineer growth and overcome the bulk solubility limits in other semiconductors alloys. Boron containing III-Nitride ternary alloys are a characteristic example: while the bulk solubility limit of B in GaN is restricted to less than 2%, B can be incorporated at the surface with contents as high as 25% forming an ordered 2×2 phase in the basal plane [3].

Surfaces and interfaces also govern the growth of semiconductor nanostructures. Nanocrystals (NCs)

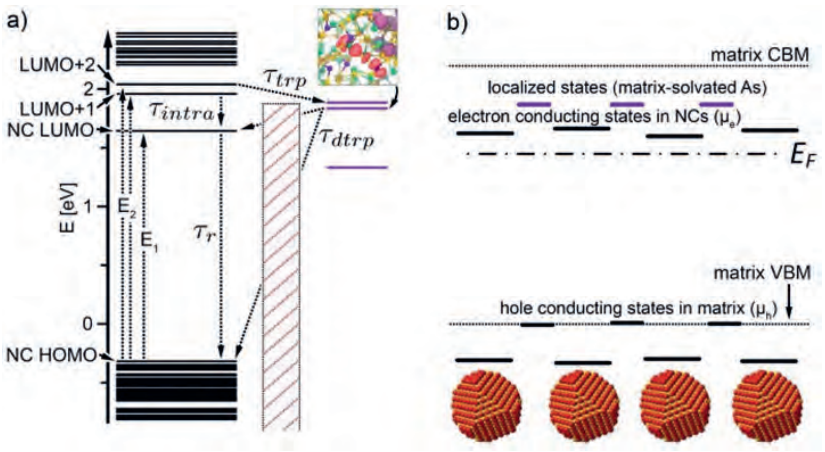

Fig. 2: *Model of ambipolar photoresponse of InAs NCs with $Sn_2S_6^{4-}$ ligands. Hot electrons promoted to the LUMO+1/+2 states can undergo intraband relaxation or get trapped by localized states that originate from matrix-solvated As, which are situated above the NC LUMO, but below the matrix conduction band edge. In the NC solid, the mobility edge for majority carriers (electrons) is associated with the NC LUMO states and the hole-conducting states are given by the matrix band edge. Copyright 2018 Nature Publishing Group.*

with controlled shape and composition can be used as "artificial atoms" to create semiconductors with superior properties, e.g., for emerging optoelectronic and photonic technologies [4]. As a prototypical example, InAs NCs are colloidally synthesized, capped with $Sn_2S_6^{4-}$ molecular metal chalcogenide complexes (MCCs), and subsequently assembled into quantum dot solids: Following solution casting and subsequent annealing, the NCs arrange in superlattice structures. After solution casting, gentle heat treatment decomposes the MCCs and results in a SnS_2 matrix encapsulating the InAs NCs. The resulting InAs/SnS_2 quantum dot solid exhibits promising transport properties, measured, e.g., by field-effect transconductance. The understanding of NC nucleation, growth, superlattice formation and assembly processes is still in its infancy, though. Often, this leads to unexpected results when process parameters are varied.

We systematically investigated the interaction of $Sn_2S_6^{4-}$ MCCs with InAs surfaces. Contrary to common assumptions drawn from studies using organic ligands, we found that the MCCs are not adsorbed as intact structural units, but rather they decompose upon contact with the NC surface, and form a passivation layer surrounding the NCs. The adsorption of intact $Sn_2S_6^{4-}$ MCCs on the passivated NP surfaces becomes then possible. However, $Sn_2S_6^{4-}$ is unstable towards dissociation into tetrahedral SnS_4 units, and the most stable structural units identified consist of passivated NCs embedded in amorphous SnS_x matrices. As an additional effect, sulphur displaces As and is incorporated into the NC subsurface layer. These theoretical predictions were later confirmed by angle-resolved X-ray photoelectron and Raman spectroscopy.

In order to model the temperature-induced decomposition of $Sn_2S_6^{4-}$ ligands adsorbed on the NC surfaces and the formation of amorphous matrices, we performed *ab initio* MD simulations where structural motifs, validated by experiments, were explicitly included as starting points of annealing cycles. We systematically explored variations in the density and stoichiometry of the amorphous matrix, generating a series of structural models of NC solids corresponding to different colloidal synthesis conditions. A number of defect states were identified that are expected to play a key role in determining the electronic and transport properties of the NC solids. We could trace the origin of the measured negative photoconductivity to the presence of As dopants: as a consequence of subsurface sulphur incorporation, As atoms diffuse into the matrix. They preferentially occupy Sn lattice sites and create localized donor states above the NC mobility edge, but below the matrix conduction band edge, cf. Fig. 2. These donor states act as traps and are responsible for the measured negative photoconductivity. By adjusting the colloidal synthesis conditions, we show how to suppress the formation of these trap states [5].

These two examples illustrate how addressing fundamental questions in semiconductor surface growth by computer simulations not only helps to rationalize experimental observations, but also to guide the design of alternative processing routes to overcome present-day compositional and defect-related limitations.

References

1. Lee, S.; Freysoldt, C.; Neugebauer, J.: Phys Rev B 90 (2014) 245301.
2. Lymperakis, L.; Schulz, T.; Freysoldt, C.; Anikeeva, M.; Chen, Z.; Zheng, X.; Shen, B.; Chèze, C.; Siekacz, M.; Wang, X.Q.; Albrecht, M.; Neugebauer, J.: Phys Rev Materials 2 (2018) 011601(R).
3. Lymperakis, L.: AIP Advances 8 (2018) 065301.
4. Wippermann, S.; He, Y.; Vörös, M.; Galli, G.: Appl Phys Rev 3 (2016) 040807.
5. Scalise, E.; Srivastava, V.; Janke, E.; Talapin, D.; Galli, G.; Wippermann, S.: Nat Nanotech 13 (2018) 841.

Solute Segregation at Grain Boundaries in Al Based on New Concepts in Machine Learning and Experiment

L. Huber [1], H. Zhao [2], R. Hadian [1], B. Gault [2], D. Ponge [2], B. Grabowski [1], J. Neugebauer [1], D. Raabe [2]

[1] Department of Computational Materials Design (CM)
[2] Department of Microstructure Physics and Alloy Design (MA)

Even very low concentrations of alloying elements can have a significant impact on the nominal material properties in a metallic alloy. One of the main mechanisms for this is the segregation of solute atoms to grain boundaries (GBs), where they can impact microstructural evolution to a degree beyond what their nominal alloying concentration would suggest. With modern experimental techniques, we are now able to measure solute concentration at particular boundaries with high accuracy [1], and can even resolve the segregation of solute atoms to particular GB sites [2]. Modelling, however, has lagged behind these developments and there is a strong need for new techniques and deeper understanding to bridge the gap between experimental measurements and atomistic simulations.

In general the solute concentration at the GB depends on the solute density of states (DOS) (i.e. segregation energies), and occupation probability for those states, which is a function of the site energy, the temperature, and the alloy composition. Here, we have developed a computational framework using classical embedded atom method potentials to evaluate the segregation energy of six different solutes to 38 unique GBs in Al – a total of more than 1.4 million segregation energies. Fig. 1(a) shows the DOS for Mg segregation aggregated across all 38 boundaries, while figs. 1(b) and (c) show examples of individual DOS for two special GBs for each solute. Alongside the DOS in fig. 1(a) we plot the corresponding Fermi-Dirac occupation curve, which takes into account that each site can be occupied by only a single atom.

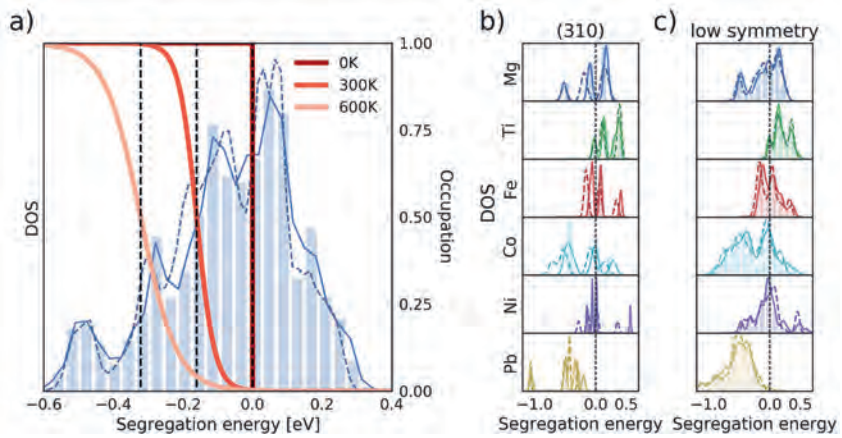

Fig. 1: *(a) The aggregated DOS across all 38 GBs for Mg segregation, as a histogram (blue bars) and smoothed distribution (solid blue line). The occupation probability at three different temperatures for a bulk concentration of 0.2 at.% (red lines) is also shown. (b and c) DOS for each of the solutes at (b) the highly-symmetric (310) GB and (c) a low-symmetry boundary. Smoothed machine-learned predictions for the DOS are shown using dashed lines in all subfigures.*

Using this rich data set, we demonstrate two new paths forward for modelling solute-GB segregation [3]. First, we have applied machine learning techniques to make accurate predictions of the segregation DOS based purely on the solute-free GB structure. This reduces the number of atomistic calculations needed to obtain the DOS for a new GB from the number of GB sites at that boundary down to one. Second, we observe that except for a few very symmetric GBs, a Gaussian distribution is often a good estimate for the DOS. With this insight, we go beyond the widely used Langmuir-McLean (LM) model by treating the DOS using its second moment, where we now have three fitting parameters instead of two – i.e. the distribution normalization, mean segregation energy, and distribution variance, instead of the LM model's saturation limit and "effective" segregation energy.

In fig. 2 we demonstrate that both the machine learning approach and Gaussian best-fit give good predictions over a broad temperature range. In contrast, the LM model – which approximates the entire segregation DOS with a single-energy Dirac-delta function – systematically fails to describe solute-GB concentration as a function of temperature. This machine learning technique opens the door to multi-scale modelling methods where larger length scales are informed by atomistic segregation data, while the Gaussian DOS approximation offers a direct link between experimental concentration measurements and atomistic simulations due to the physical interpretability of its fit parameters.

In parallel, we have used atom probe tomography (APT) to study segregation at Σ13(001) GBs in an Al-6.22%Zn-2.46%Mg-2.13%Cu alloy (wt.%), which

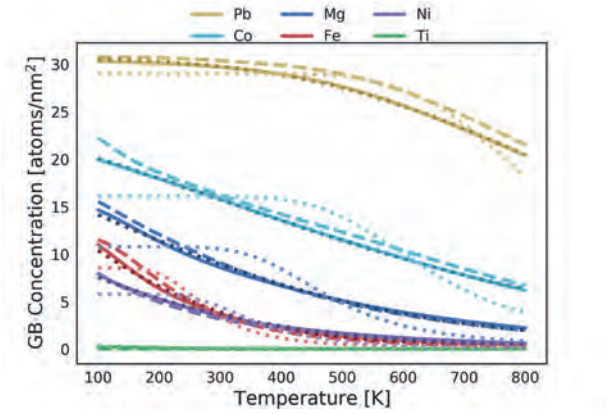

Fig. 2: *Solute-GB concentration isotherms at the GB for all six solutes with a nominal concentration of 0.2 at.%. Results are shown for calculated segregation energies (solid lines), machine-learned energies (dashed lines), Langmuir-McLean best-fit (light dotted lines), and Gaussian best-fit (dark dotted lines).*

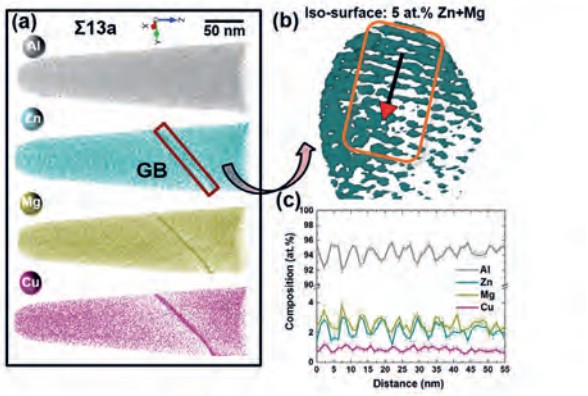

Fig. 3: *Atom probe tomography results obtained on a Σ13 GB in the as-quenched state: (a) Atom maps of all elements; (b) Distribution of solutes within the grain boundary (region indicated by the red rectangle in (a)); (c) Corresponding one-dimensional composition profile along the arrow in (b).*

belongs to the high strength Al-7XXX series. To begin, we solution heat treated the material at 475°C for 1 hour before water quenching [4]. We then prepared APT samples using a FEI Helios plasma focused ion beam (PFIB) with a Xe source and acquired near-atomic-scale compositional information using a Cameca LEAP5000XR local electrode atom probe instrument. With a conventional Ga source for FIB, the quality of atom probe data is compromised by the strong segregation of Ga to Al GBs, which also leads to embrittlement. The use of the Xe-source has allowed us to obtain the first ever set of reliable APT data for grain boundary composition in Al-alloys.

Analysis of one of the resulting APT measurements for the as-quenched Al-Zn-Mg-Cu alloy is shown in fig. 3. The location of the GB is highlighted with a red box in fig. 3(a), while isosurfaces of 5 at.% Zn+Mg are shown in fig. 3(b) for the cross sectional slice from this region. Fig. 3(a) demonstrates that all solute species, i.e. Zn, Mg, and Cu, have already segregated to the GB by the end of the quench. We see in fig. 3(b) that this segregation follows periodic patterns throughout the entire GB. These segregation patterns are formed due to the preferential segregation of Zn and Mg to particular sites, similar to observations from our simulations. The corresponding composition profile along the pattern axis is shown in Fig. 3(c). A periodic distribution is revealed, with 5 nm distance between the peaks. The segregation patterns and compositional analysis indicate that this phenomenon can be related to the periodic alternating structure within the grain boundary [2] or faceted grain boundary as Liebscher et al. studied in multicrystalline Si [5]. Facetted boundaries can be studied using our computational methodology in a piece-wise fashion, and we plan to extend our research in this direction.

Going forward, a deeper integration of these cutting edge experimental and simulation techniques will be used to advance our understanding of solute segregation at GBs. As indicated by our simulation work, the GB normal plane can have a strong influence on the amount of segregation. In light of this observation, we will perform further experiments which fully characterize all five GB parameters. This will allow us to directly compare both the degree of segregation and its spatial patterning as predicted by theory and observed in experiment.

References

1. Herbig, M.; Raabe, D.; Li, Y.J.; Choi, P.; Zaefferer, S.; Goto, S.: Phys Rev Lett 112 (2014) 126103.
2. Nie, J.; Zhu, Y.; Liu, J.; Fang, X.-Y.: Science 340 (6135) (2013) 957.
3. Huber, L.; Hadian, R.; Grabowski, B.; Neugebauer, J.: npj Comp Mat 4 (2018) 64.
4. Zhao, H.; De Geuser, F.; da Silva, A.K.; Szczepaniak, A.; Gault, B.; Ponge, D.; Raabe, D.: Acta Mater 156 (2018) 318.
5. Liebscher, C.; Stoffers, A.; Alam, M.; Lymperakis, L.; Cojocaru-Mirédin, O.; Gault, B.; Neugebauer, J.; Dehm, G.; Scheu, C.; Raabe, D.: Phys Rev Lett 121 (2018) 015702.

Magnetic Disorder in Materials: *Ab initio* Methods and Applications

I. Stockem, O. Hegde, O. Waseda, C. Freysoldt, T. Hickel

Department of Computational Materials Design (CM)

A majority of the material systems investigated at the MPIE, including for instance advanced high-strength steels, Ni-based superalloys, high-entropy Cantor alloys or magnetocaloric alloys, show magnetism at the atomic scale. Ferromagnetic or other ordered magnetic configurations, that form the ground state of the material, are nowadays routinely computed in density functional theory (DFT). In technological applications most of the above mentioned materials are, however, operating well above their ordering temperature. Consequently, the magnetic entropy yields highly disordered (i.e. unstable) magnetic configurations and high-frequency fluctuations, which are not captured in conventional DFT calculations.

In the CM department, employing our own DFT code S/PHI/nx gives us the chance to implement and apply techniques tailored for these challenges. In the group of C. Freysoldt a novel way of constraining the local magnetic density to atomic moments of arbitrary magnitude and direction was developed [1]. It uses the concept of Lagrange multipliers, similarly to the way a normalization of the wave function is ensured during the electronic structure minimization cycle. Extensive performance tests revealed that this approach yields substantially faster and more stable convergence than the consideration of penalty terms with auxiliary magnetic fields implemented in other codes. In this way, magnetic disorder in materials from steels up to Fe-based superconductors became accessible.

The fluctuations in the magnetic disorder have been addressed with two different strategies: The spin-space averaging (SSA) technique has been developed by F. Körmann [2] to simulate phonons in the paramagnetic regime. It is based on the assumption that the changes in the magnetic configurations occur on a much shorter time scale than the atomic vibrations. An average over all magnetic configurations contained in a supercell, in which up- and down spins are distributed according to the concept of special quasirandom structures (SQS), simulates the magnetic fluctuation, but preserves the structural symmetries. The SSA approach quantitatively reproduces the experimentally observed softening of phonons when heating the material across the magnetic transition temperature.

Based on this success, the group of T. Hickel applied the SSA technique for the relaxation of atoms next to structural defects in paramagnetic materials. It is fully clear that a single disordered magnetic structure would yield artificial forces that are inconsistent with the structural symmetry. To make the averaging of forces during the relaxation efficient, several synchronous DFT calculations, an on-the-fly averaging of forces and an external structure optimization have been employed. The combination of different codes and the implementation of the complex simulations protocol were substantially simplified by using pyiron, the novel integrated development environment of the CM department (see p. 48).

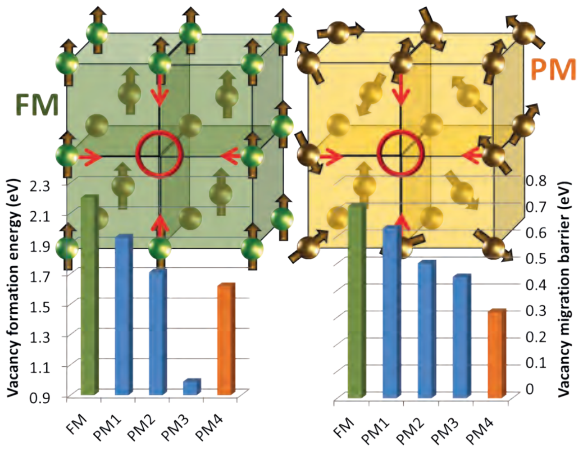

Fig. 1: *Vacancy formation (left) and migration (right) energies in the ferromagnetic (FM) and paramagnetic (PM) state. In the PM state no relaxation (PM1), a ferromagnetic relaxation (PM2), a relaxation of individual paramagnetic snapshots (PM3) and a relaxation according to averaged paramagnetic forces (PM4) are compared.*

The application of this technique to vacancies in bcc Fe yields remarkable relaxation effects. It turns out that the formation as well as the migration energy are substantially reduced by magnetic disorder (compare FM and PM2 in Fig. 1). More importantly, however, the correct relaxation of the atomic positions yields an additional reduction of these energies by the same order of magnitude (compare PM1 and PM4 in Fig. 1). Therefore, using relaxations in ordered magnetic states for the determination of paramagnetic vacancy formation energies (PM2 in Fig. 1) fails to be accurate.

The second strategy to consider magnetic fluctuations is the application of atomistic spin dynamics (ASD) at finite temperatures. This approach becomes particularly attractive if combined with *ab initio* molecular dynamics (AIMD). For this purpose, I. Stockem [3] has developed in a close collaboration with Linköping University (B. Alling) an alternating scheme (Fig. 2), in which every ASD step receives an updated set of atomic positions and therewith

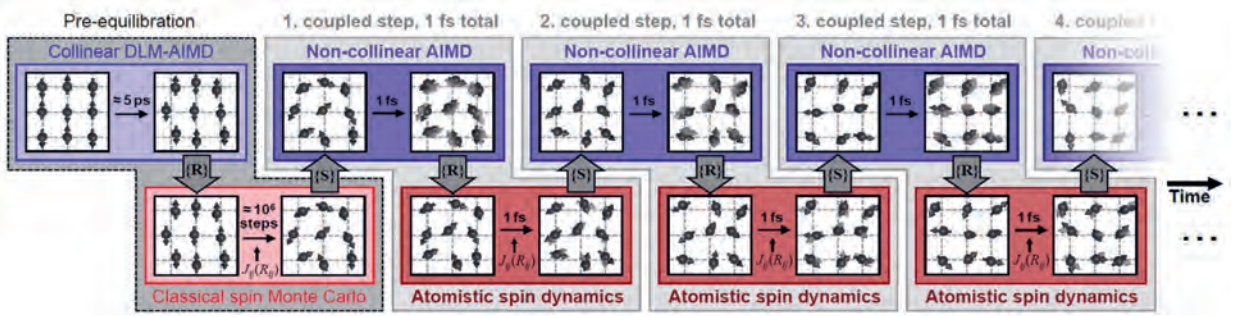

Fig. 2: *Alternating scheme, combining ab initio molecular dynamics (AIMD) for disordered local moments (DLM) with atomistic spin dynamics.*

magnetic interaction parameters, and every AIMD step receives an updated set of magnetic moments, which are constrained during the *ab initio* calculation of forces. In this way mutual coupling effects become accessible.

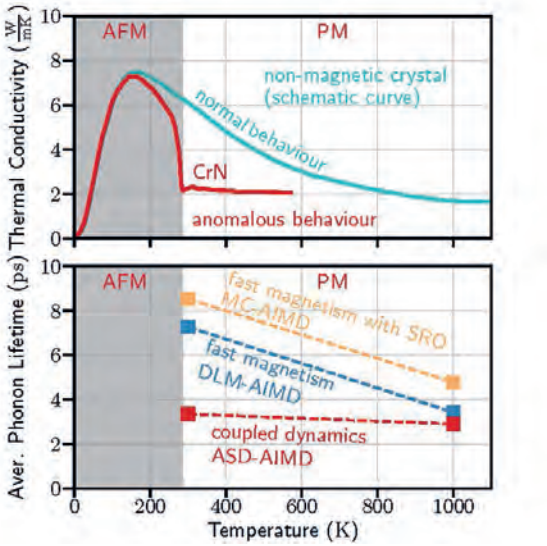

Fig. 3: *Experimentally observed anomaly of the hermal conductivities of CrN (top) compared to the averaged phonon lifetime as obtained with different simulation techniques (bottom).*

Indeed, the application of this scheme to CrN has lead to interesting insights: Although there is no long-range magnetic order in the paramagnetic state, the spin orientations of neighbouring Cr atoms depend clearly on the distances of these atoms: As two neighbouring Cr atoms approach during the vibration, their spins tend to point into opposite directions. If they are further away from each other, the corresponding spins prefer an orientation into the same direction. Furthermore, the mutual coupling of the spin orientations and the distance between the neighbouring Cr atoms prevents the spin system from a fast decay compared to the spin dynamics of an uncoupled vibrating lattice.

We studied the influence of this dynamic coupling on phonon lifetimes in CrN. The relevance of short range order (SRO) effects are highlighted by a comparison with alternative methods (Fig. 3): If the directions of the magnetic moments are randomly changed at each step (DLM-AIMD), the magnetic subsystem shows no SRO, neither in space nor time. If the atomic configurations are determined by Monte-Carlo simulations, the spins exhibit a temperature-dependent SRO in space, but not in time. We realize that only our coupled ASD-AIMD approach, which includes SRO in space and time, yields a vanishing temperature dependence of the resulting phonon lifetimes. This explains an anomalous temperature dependence of the thermal conductivity of CrN in its paramagnetic state, which was observed experimentally, but not understood before (Fig. 3).

References

1. Grabowski, M.: Master thesis, Heinrich-Heine-Universität Düsseldorf (2015).
2. Körmann, F.; Grabowski, B.; Dutta, B.; Hickel, T.; Mauger, L.; Fultz, B.; Neugebauer, J.: Phys Rev Lett 113 (2014) 165503.
3. Stockem, I.; Bergman, A.; Glensk, A.; Hickel, T.; Körmann, F.; Grabowski, B.; Neugebauer, J.; Alling, B.: Phys Rev Lett 121 (2018) 125902.

Applying an *ab initio* Potentiostat to Elucidate the Fundamental Mechanism behind Mg Corrosion

S. Surendralal [1], M. Todorova [1], S. Wippermann [2], J. Neugebauer [1]

[1] Department of Computational Materials Design (CM)
[2] Department of Interface Chemistry and Surface Engineering (GO)

Solid/liquid interfaces are at the heart of many applications of practical importance. Examples are batteries, electro catalysis, fuel cells or corrosion. To understand and eventually overcome the technological challenges faced in these applications requires accurate modelling techniques. Electronic structure calculations are free of fitting parameters and provide insights at the atomistic level. They are thus the method of choice, provided that we are able to overcome the issues impeding the modelling of constant electrode potential conditions, essential for the realistic description of solid/liquid interfaces. We recently developed a method that successfully addresses these issues (see p. 47) and provides an *ab initio* potentiostat [1], thus enabling calculations under applied bias in complete analogy to electrochemical experiments.

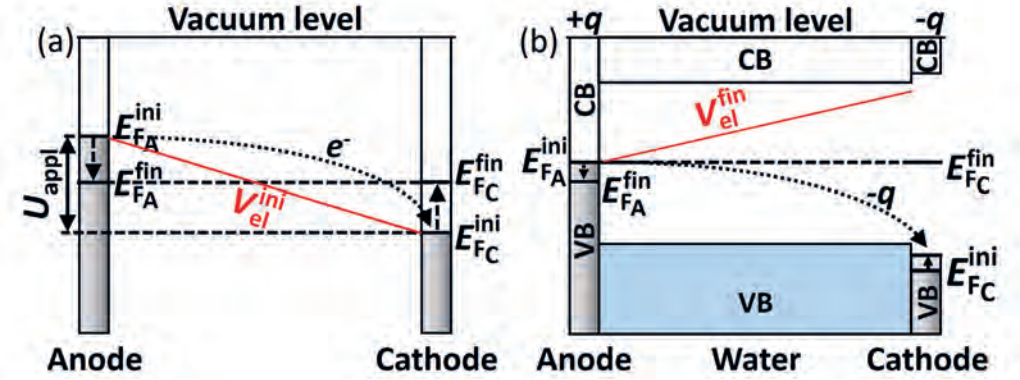

Fig. 1: *Schematic representation of the concept used to realize an electrolytic cell. (a) Alignment between two metal electrodes before (superscript "ini") and after (superscript "fin") charge transfer. The charge transfer leads to equal Fermi energies E_F, preventing the realization of an electric field. The red line shows the electrostatic potential before the charge transfer. (b) A doped semiconductor electrode allows us to control the position of the Fermi level. The type (here, p type) and concentration of dopants controls the polarity and magnitude of the field. The red line shows the electrostatic potential realized by the charge transfer. The slope of the potential is proportional to the induced electric field.*

We had to overcome two key challenges. To ensure a constant electrode potential *U* electrons are transferred from the anode (positively charged electrode) to the cathode (negatively charged electrode). The ensuing electric field drives negatively charged ions, such as OH^-, to the positively charged anode and positively charged ions, such as H^+ (protons), to the negatively charged cathode. This means that electrodes are thermodynamically open to both electrons and protons, and thus fundamentally grand canonical. This is difficult to realize in a standard density functional theory (DFT) code where the particles and electrons in the cell remain constant. However, a full electrolytic (or electrochemical) cell contains both the positively and the negatively charged electrode and is canonical for both electrons and protons. By realizing a canonical setup in a DFT calculation we retain a constant number of electrons and protons throughout the calculation and circumvent the described difficulty. This setup enables us to describe a realistic electrochemical system, if we are able realize an electric field between the two electrodes. This is challenging in a standard DFT code with periodic boundary conditions, because the necessity of having a different Fermi level on each electrode, a requirement to realizing a potentiostat and thus an electric field between the two electrodes, contradicts the mandatory condition for a constant Fermi level throughout a cell (see Fig.1a). To overcome this fundamental limitation while still using a standard DFT code we introduced a novel type of computational electrode by replacing one of the metal electrodes by a doped semiconductor (Fig.1b). In cases where the semiconductor is not doped and the Fermi level of the metal electrode falls within the band gap of the semiconductor electrode the two electrodes are decoupled and there is no charge transfer between them. If we dope the semiconductor electrode *p*-type the ensuing charge transfer from the metal electrode will charge the semiconductor negative and make it the cathode, as seen in Fig.1b. Conversely, doping the semiconductor electrode *n*-type will result in charge transfer to the metal electrode, charging the semiconductor electrode positive and making it

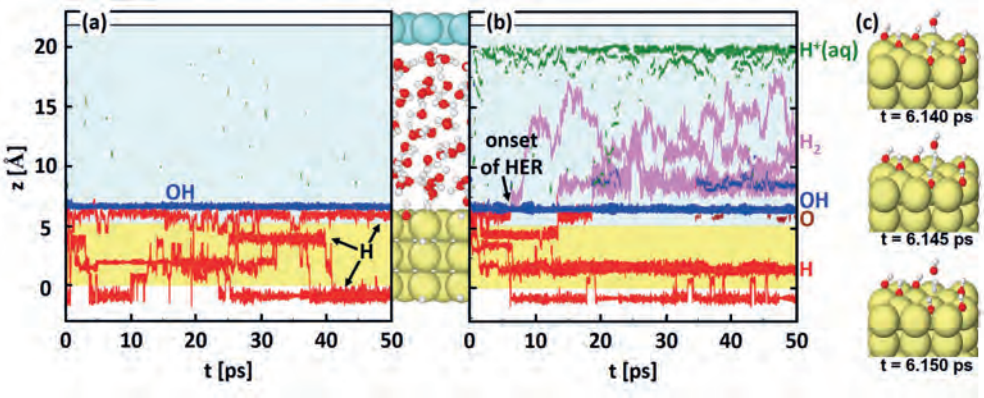

Fig. 2: *Ab initio computed trajectories of the atomic and molecular species formed when Mg is exposed to water for (a) open circuit conditions and (b) applying a linear increasing voltage. Trajectories are shown in a projection along the normal to the Mg surface. Blue, red, violet, green, and brown lines mark OH, H, H_2, H^+(aq.), and O, respectively. The onset of the H_2 evolution reaction is indicated in (b) by a black arrow. To focus on the relevant reaction products Mg-water trajectories are shown as yellow (blue) colored background. The atomic geometry of the electrolytic cell is visualized in the figure between (a) and (b). Atoms are shown as colored spheres: Mg (yellow), Ne (turquoise), oxygen (red), hydrogen (gray). (c) Snapshots of the HER extracted from the MD trajectory of the system under applied bias potential.*

the anode. The charge transfer induces a potential bias *U* and an electric field. Controlling the doping charge *q* enables us to control the bias and the field.

We identified Ne as the most suitable semiconductor electrode, as it possesses the following characteristics: (i) its band gap, although significantly reduced in DFT calculations, remains sufficiently large and is suitably aligned, (ii) Ne is van der Waals bonded and has a negligible deformation potential, (iii) it is chemically inert, so that chemisorption or alloy formation at the electrode are suppressed, (iv) even a single layer of Ne prevents permeation of water molecules and its residues. To dope the Ne electrode we use pseudo-atoms with fractional proton numbers. This gives us flexibility regarding the charge on the electrode by not restricting us to integer numbers, as explicit dopants would have. The full control we retain over the electrode charge is a central element to constructing a static or dynamic potentiostat.

Utilizing pyiron (see p. 48) allowed us to implement a charge control feedback-loop outside the DFT code. This way we can employ the new approach with any DFT code and without having to make changes to the underlying code. We were thus able to employ a standard DFT code (VASP) to study one of the key puzzles in corrosion science – the anomalous hydrogen evolution at an anodically polarized Mg electrode. According to fundamental corrosion concepts, H_2 evolution should occur only at the negatively charged cathode via a reaction consuming electrons, i.e. $2H^+ + 2e^- \rightarrow H_2$. The counterintuitive behaviour observed at anodically polarized Mg in contact with water has been known for 150 years, but the atomistic mechanism of the reaction is yet unknown. At open circuit conditions, i.e. without an applied electric field, we observe spontaneous dissociation of water molecules at the Mg surface (cf. Fig. 2a) and a subsequent adsorption of OH on the surface up to a maximum coverage of 1/3 ML (monolayer), but no H_2 formation. Following anodic polarization of Mg (cf. Fig. 2b) the OH coverage increases to 1 ML and we observe H_2 evolution. Since our *ab initio* setup allows us to inspect the reaction at the atomic level, we extract relevant snapshots from the molecular dynamics trajectory (see Fig. 2c) to study the reactions. As can be seen, a water molecule binds to an H atom adsorbed on the Mg surface, dissociates and leaves a H_2 molecule and an OH^- ion. While this reaction looks like a "conventional" Heyrovsky reaction in an alkaline medium, $H_{ad} + H_2O + e^- \rightarrow H_2 + OH^-$, its occurrence at the anode, where electrons are deficient, contradicts present concepts in electrochemistry. A careful inspection of the electronic structure reveals that, even under the condition of a positively charged Mg surface, the adsorbed H is not charge neutral, but negatively charged H^-. Thus, H itself, rather than the anode provide the required excess electron, and the ensuing reaction becomes $H^-_{ad} + H_2O \rightarrow H_2 + OH^-$. In the absence of a potential (open circuit conditions), the reaction does not occur [see Fig. 2(a)], because the attractive electrostatic interaction between the OH^- ion and the anode, which is critical to make this reaction exothermic, is absent. Being able to unravel this long standing corrosion science question shows the power of the new potentiostat approach and its potential to address a wide range of questions related to electrochemistry and corrosion.

References

1. Surendralal, S.; Todorova, M.; Finnis, M.W.; Neugebauer, J.: Phys Rev Lett 120 (2018) 246801.